Article

Optimized Design and Experimental Evaluation of a Ridging and Mulching Machine for Yellow Sand Substrate Based on the Discrete Element Method

Yi Zhu [1,2,3], Jingyu Bian [1,2,3], Wentao Li [1,2,3,*], Jianfei Xing [1,2,3,4], Long Wang [1,2,3], Xufeng Wang [1,2,3] and Can Hu [1,2,3]

[1] College of Mechanical and Electrical Engineering, Tarim University, Alar 843300, China; wxf@taru.edu.cn (X.W.)

[2] Xinjiang Production and Construction Corps Key Laboratory of Utilization and Equipment of Special, Alar 843300, China

[3] Modern Agricultural Engineering Key Laboratory, Universities of Education Department of Xinjiang Uygur Autonomous Region, Alar 843300, China

[4] College of Engineering, China Agriculture University, Beijing 100083, China

[*] Correspondence: 10757231177@stumail.taru.edu.cn

Abstract

Conventional ridging and mulching machines struggle to perform effectively in yellow sand substrates due to their loose texture, high collapsibility, and strong fluidity, which compromise ridge stability and operational quality. To address these challenges, this study proposes the development of an integrated rotary tillage, ridging, and film-mulching machine specifically designed to meet the agronomic requirements of tomato cultivation in greenhouse environments with yellow sand substrate. Based on theoretical analysis and parameter calculations, a soil transportation model was established, and the key structural parameters—such as blade arrangement and helical shaft geometry—were determined. A discrete element method (DEM) simulation was employed to construct a contact model for the yellow sand–slag mixed substrate. A combination of single-factor experiments and Box–Behnken response surface methodology was used to investigate the effects of forward speed, shaft rotational speed, and tillage depth on ridge stability and operational performance. The simulation results indicated that a forward speed of $0.82 \text{ m} \cdot \text{s}^{-1}$, shaft speed of 260 rpm, and tillage depth of 150 mm yielded the highest ridge stability, with an average of 95.7%. Field trials demonstrated that the ridge top width, base width, height, and spacing were 598.6 mm, 802.3 mm, 202.4 mm, and 1002.8 mm, respectively, with an average ridge stability of 94.3%, differing by only 1.4 percentage points from the simulated results. However, a quantitative traction/energy comparison with conventional equipment was not collected in this study, and we report this as a limitation. The energy consumption is estimated based on power usage and effective field capacity (EFC) under similar operating conditions. Soil firmness reached 152.1 kPa, fully satisfying the agronomic requirements for tomato cultivation. The proposed machine significantly improves operational adaptability and ridge stability in yellow sand substrate conditions, providing robust equipment support for efficient greenhouse farming.

Keywords: yellow sand substrate; ridge-forming and mulching machine; discrete element method simulation; field experiment

1. Introduction

Yellow sand is widely distributed across arid and semi-arid regions, and is composed primarily of loose sand particles with weak cohesion and a poorly developed aggregate structure. These characteristics result in low water and nutrient retention capacity, and make the substrate prone to displacement under mechanical disturbance or wind erosion, thereby compromising its overall stability [1,2]. To improve agricultural productivity in saline-alkali desert regions, especially in arid zones of northwestern China such as Xinjiang, a "yellow sand-based soilless cultivation" system has been promoted. This system employs a layered substrate composed of yellow sand and slag, combined with drip irrigation, to enhance crop yield and resource-use efficiency [3–6]. However, the high fluidity and loose structure of yellow sand substrates pose significant challenges for mechanical operations such as ridging and mulching, making it difficult to maintain ridge stability and thus limiting the quality of mechanized farming.

In recent years, the integration of multifunctional capabilities and structural lightweighting of mechanical equipment has become a significant trend in greenhouse environments [7]. For example, integrated ridging–mulching–drip irrigation machines and multifunctional ridging–disinfection devices have been proposed, showing that combining multiple processes in a compact space can significantly improve efficiency and adaptability [8,9]. These advancements highlight the research frontier of multifunctional greenhouse machinery. Within this context, the ridging and mulching machine developed in this study represents an innovative exploration aimed at meeting the unique demands of yellow sand substrates.

Existing ridging and mulching machines demonstrate insufficient adaptability in sand-based cultivation environments. Conventional traction-type ridgers frequently fail to form stable ridges, as the high dispersibility of sand particles leads to loosely shaped ridges with poorly defined boundaries. Field experience, such as tomato cultivation in solar greenhouses in southern Xinjiang, indicates that current equipment often results in discontinuous operations, high tillage omission rates, and reduced efficiency. Constant-pitch ridging rollers [10], commonly employed in practice, exacerbate this issue by inducing uncontrolled particle dispersion, making directional soil conveyance difficult and producing unstable ridge profiles. Consequently, the mulching film cannot adhere tightly to the substrate surface, reducing the effectiveness of ridging and mulching and adversely affecting the crop microenvironment.

The discrete element method (DEM) has been extensively applied to study soil-machine interactions and optimize agricultural machinery [11–13]. Reviews and comparative studies have emphasized how contact model selection strongly affects simulation fidelity and operational performance [14–16]. In China, structural optimization studies have further advanced DEM applications: spiral soil-covering drums for mulching seeders [17], parameter calibration of sandy substrates [18,19], DEM-based potato–soil separation devices [20], and optimization of ridging–fertilizing modules in arid zones [21,22]. Although such studies provide valuable references, research focusing specifically on yellow sand substrates remains scarce.

Although these studies have provided valuable references for the mechanization of yellow sand substrates, research specifically targeting yellow sand substrates remains in its infancy. Under low moisture conditions, yellow sand exhibits almost no intrinsic cohesion; however, in an unsaturated state, the matric suction and liquid bridge effects impart weak apparent cohesion and tensile strength to the system, thereby enhancing the self-supporting capacity of the pile structure in the short term [23]. Therefore, in this study, a slight degree of bonding was introduced in the DEM model to represent this weak cohesion. The tillage depth and target ridge height were then optimized within the stability zone that maintains weak cohesion. Simultaneously, the contact and friction parameters of the sandy soil were

inversely calibrated using measurable macroscopic indicators [24]. Following the method proposed by Zhang Rui et al. [25] for DEM parameter calibration of sandy soils, the model was first calibrated to match the simulated repose angle with the measured value, and the bonding strength was then fine-tuned within the weakly cohesive framework to ensure the stability of both the ridge and pile structures.

In the cultivation environment using yellow sand as the substrate, its high flowability often leads to unstable ridge structures, and ridge collapse is common during mechanical operations [26]. Additionally, in low-cohesion sandy soils, the reduced friction at the film–soil interface results in insufficient film tension and surface wrinkling during the laying process, significantly affecting the mulching effectiveness [27]. Previous studies have shown that the frictional properties of the film material directly affect the transmission of tension and its stability [28]. To address these issues, this study proposes an innovative design aimed at enhancing the film tension and improving the film–soil interface adhesion, thereby improving the mulching performance and solving the technical challenges in yellow sand-based substrates.

To address the technical challenges outlined above, this study proposes an innovative solution based on the dynamic properties of yellow sand substrate particles. A composite roller system, incorporating variable-pitch ridging blades and rotary tillage blades, is designed. By gradually changing the helix angle and pitch along the axis of the roller, the yellow sand substrate is directed and dispersed progressively under the action of the rotating blades. Through discrete element method (DEM) simulations and field experiments, the results demonstrate that this design significantly improves the aggregation state of yellow sand particles, leading to more compact and stable ridge formation.

2. Materials and Methods

2.1. Agronomic Requirements

Native yellow sand's high permeability and low water-holding capacity frequently make traditional soil-based cultivation in northwest China's arid regions impossible, usually requiring expensive soil replacement techniques. In this study, industrial slag and locally available yellow sand were combined at a mass ratio of 5:3 to create a cultivation substrate. The slag used was a by-product of local industrial silicon smelting, which was crushed and sieved to obtain porous particles with an average size of approximately 2 mm. This composite substrate exhibits a loose structure and favorable porosity, greatly improving the water retention and reducing excessive permeability compared to pure yellow sand. The enhanced physical properties enable direct planting without the need for soil replacement, thereby reducing soil amendment costs and improving overall cultivation efficiency [29].

The term "ridge" herein refers to a raised, strip-shaped soil structure formed on the surface at specified widths and intervals. As illustrated in Figure 1, the ridge design includes a ridge top width (L_1) of 600 mm, a ridge base width (L_2) of 800 mm, an inter-ridge spacing (L_3) of 1000 mm, and a ridge height (H) of 200 mm, with a ridge side slope angle (α_r) of 56°. This ridge configuration reduces deep percolation losses through capillary barrier effects. Additionally, plastic film mulching suppresses evaporation and weed growth by maintaining lower soil temperatures, while the integrated drip irrigation system delivers precise water application. Together, these practices contribute to microclimate modification beneath the mulch, promoting early crop maturity and yield enhancement.

2.2. Machine Structure and Working Principle

In order to improve ridge formation stability and operational consistency, this study presents design optimizations in both the cutting process and DEM-based modeling to

address the distinct physical properties of yellow sand substrates [30]. To satisfy the requirements of cultivation based on yellow sand, a specific mulching and ridging equipment was created. To increase adaptability in such demanding circumstances, the machine's architecture and parameter settings were methodically tuned. By combining rotary tillage, ridging, shaping, drip tape laying, and plastic film mulching into a single pass, as shown in Figure 2, the multipurpose machine significantly lowers cultivation costs and boosts productivity, offering strong equipment support for sustainable agriculture in arid regions.
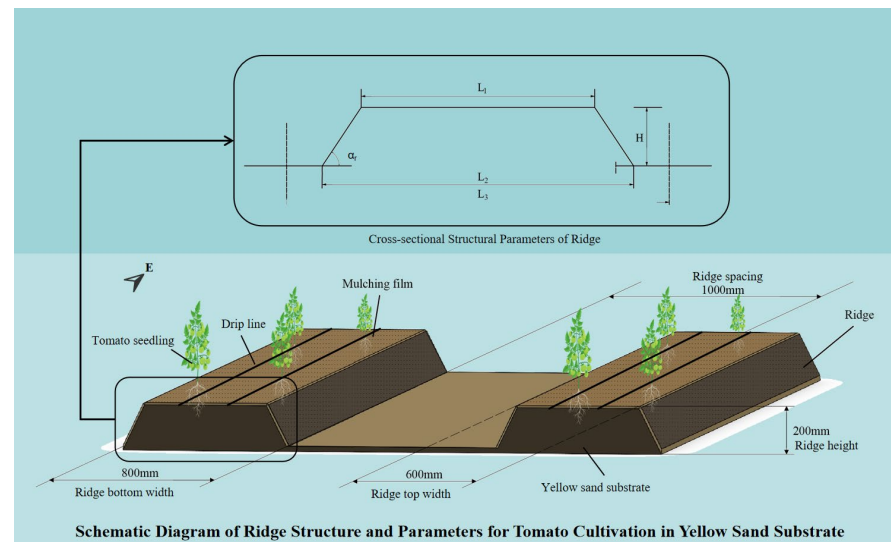

Figure 1. Structural configuration and parameters of the ridge profile for tomato cultivation in yellow sand substrate.
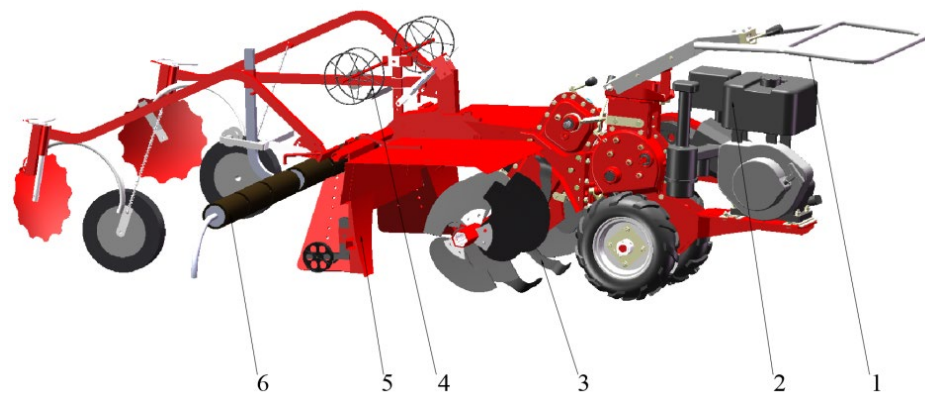

Figure 2. Structural schematic of the ridge-forming and film-mulching machine: 1 walk-behind tractor; 2 gasoline engine; 3 ridging mechanism; 4 drip irrigation tape laying mechanism; 5 shaping mechanism; 6 film-mulching mechanism.

The machine comprises several key components: a walk-behind tractor (1), a gasoline engine (2), a ridging mechanism (3), a shaping unit (5), a film mulching system (6), and a drip tape laying mechanism (4). Power from the gasoline engine is transmitted via a V-belt to the main gearbox of the tractor, then transferred through sprockets to a gear distribution box, which in turn powers the gearbox of the ridging unit. The ridging blade roller fractures the yellow sand substrate through cutting, throwing, and impact actions, concentrating the soil toward the center. The shaping unit further refines the soil to conform to the specified ridge profile. The film mulching system, attached to the shaping unit via a friction-based clamping mechanism, rotates synchronously with the unit during operation. It spreads the plastic film evenly over the ridge, while press wheels firmly secure the film edges to ensure proper adhesion. Plowshares mounted on the shaping board direct yellow sand

from the furrow onto both sides of the film, and covering discs then apply a soil layer over the film edges to complete the mulching process. A cutting blade at the end of the mulching mechanism severs the film, preparing the machine for the next operational cycle. The drip irrigation tape reel is mounted along the central axis of the implement, allowing the tape to be laid simultaneously with the mulching process, thereby preventing lateral deviation. Prior to mulching, a guiding slot is designed to lead the tape onto the ridge crest, after which the plastic film covers and secures it in place. This arrangement ensures that the drip irrigation tape remains naturally fixed at the ridge center and minimizes the risk of displacement. The specifications of the machine are shown in Table 1.

Table 1. Specifications of the ridge-forming and film-mulching machine.

Parameter	Value
Supporting power, kW	≥ 10
Large/small ridge width, mm	700–1000
Large/small ridge height, mm	150–300
Number of working rows, rows	1
Film width, mm	1200–1500
Number of rotary tiller blades, pcs	6
Number of ridging blades, pcs	12
Rotary tillage depth, mm	180~220
Operating speed/(km·h^{-1})	2–3

2.3. Key Component Design

2.3.1. Ridging Mechanism

Figure 3 illustrates the development of a new rotary-based dynamic ridging system that incorporates a compound soil-forming mechanism specifically designed for yellow sand substrate conditions. Six ridging blades and three rotating tillage blades on each side make up the device's symmetrical design, which is placed in variable-pitch helical patterns to effectively fragment, move, and shape the substrate. In order to converge the dirt toward the center, where more central blades further crush and aggregate the material, the rotary blades are mounted on two shafts and arranged in counter-helical orientations.
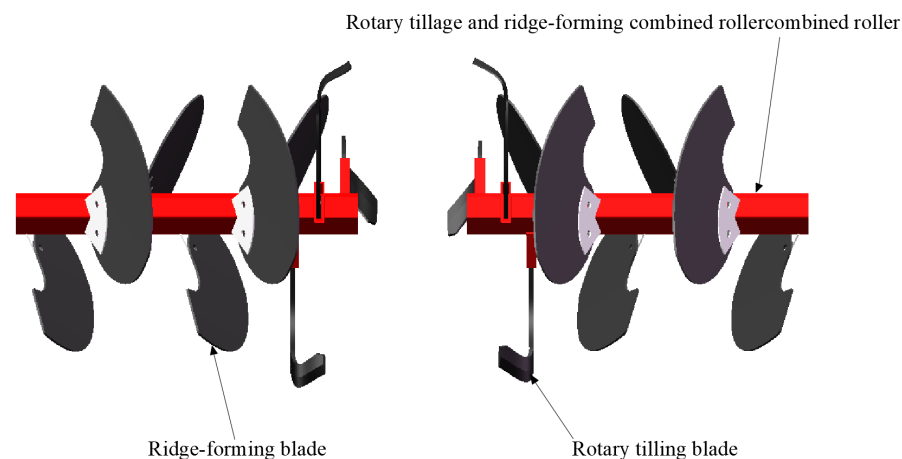

Rotary tillage and ridge-forming combined rollercombined roller

Ridge-forming blade

Rotary tilling blade

Figure 3. Arrangement of rotary–ridging blades.

To enhance the ridge's geometric stability and forming accuracy, the pitch of the ridging blades gradually decreases from the outer to the inner region. This is complemented by a tunable contouring mechanism that compacts and profiles the concentrated soil to form a high-density, uniform ridge. Additionally, larger-diameter rotary blades are employed near the gearbox area to reduce traction resistance during operation.

2.3.2. Mathematical Model for Helical Transport of Yellow Sand Substrate

One important aspect affecting the stability and quality of ridge development is the rotary ridging mechanism's transport capacity for yellow sand substrate. To direct the structural optimization of soil-working components, a theoretical model of this process must be established. Dual variable-pitch helical conveyors are created in this method by symmetrically mounting the ridging blades on the central shaft. These conveyors push the substrate inward from both lateral sides.

During operation, the transport rate of the substrate varies along the axial direction; as it approaches the ridge center, both the blade pitch and flow rate increase, leading to accelerated axial transport. Conventional ridging machines typically adopt constant-pitch designs sized for peak transport demand, resulting in unnecessary power consumption in under-utilized regions. To overcome this inefficiency, the proposed ridging mechanism employs a variable-pitch blade configuration, where a larger pitch near the inlet enhances substrate capture, and a smaller pitch near the outlet promotes effective compaction—together improving overall transport efficiency and operational precision.

According to the dynamics of the yellow sand substrate, the tool-substrate interaction can be split into two phases: the cutting and crushing phase, when the tool edge breaks up the soil matrix, and the transportation and accumulation phase, when the rotary motion helps the broken material move forward. Based on the principle of kinematic similarity, the compound motion of the tool is decomposed into the synergistic effects of unidirectional advancement and radial throwing, thereby establishing an equivalent analytical model for the helical conveying process. By introducing a dynamic correction factor to adapt the conventional screw-conveying theory, a three-dimensional conveying model is developed, incorporating the physical properties of the yellow sand substrate, the geometric parameters of the tool, and the kinematic conditions. This model significantly enhances the description of the nonlinear relationship between near-contact accumulation and bulk transport quality, providing a theoretical basis for optimizing the structural parameters of the tillage components and for constructing an equivalent analytical model of the helical conveying mechanism.

$$Q_1 = \mu Q_2 \tag{1}$$

where Q_1 is the actual transport rate of the yellow sand substrate achieved by the ridging mechanism (t·h^{-1}); Q_2 is the theoretical transport capacity of a standard open-pitch screw conveyor (t·h^{-1}); μ is an empirical correction coefficient accounting for dynamic flow irregularities, incomplete filling, and the interactive effects between soil particles and the blade surface.

The theoretical throughput Q_2 of the open-type helical conveyor can be calculated as

$$Q_2 = 3600 F V_Z \sigma \tag{2}$$

where F is the effective cross-sectional area for material transport (m^2); V_Z is the axial transport velocity of the substrate (m·s^{-1}); ρ is the bulk density of the yellow sand substrate (t·m^{-3}), experimentally measured as 1.4 t·m^{-3}; σ is the inclination correction coefficient, typically taken as 0.3 for low-cohesion materials such as sand.

Based on the comprehensive material property coefficient, σ was set to 0.3, and the measured bulk density ρ was determined to be 1.4.

$$F = \frac{\varphi D^2 \pi}{4} \tag{3}$$

where φ is the fill coefficient (dimensionless); D is the diameter of the ridging blade shaft drum, m.

In practical applications, the influence of axial resistance on substrate movement is often negligible. Hence, the axial velocity V_Z can be approximated as

$$V_Z = \frac{d_z}{d_t} = \frac{d\left(\frac{S\omega T}{2\pi}\right)}{dt} = \frac{S\omega}{2\pi} = \frac{Sn}{60} \tag{4}$$

where S is the helical pitch of the blade, m; n is the rotational speed of the shaft, rpm.

Substituting Equations (2) and (3) into Equation (1), the actual substrate throughput Q_1 is reformulated as

$$Q_1 = 47\mu D^2 Sn\rho\sigma \tag{5}$$

As illustrated in Figure 1, the cross-sectional area A of the ridge consists of two geometric components: a trapezoidal base and a semi-elliptical top. The total area is expressed as

$$A = \frac{(L_1 + L_2)H}{2} \tag{6}$$

where A is the cross-sectional area of the ridge, mm^2; L_1 is the ridge top width, mm; L_2 is the ridge base width, mm; H is the ridge height, mm.

The actual cross-sectional area A_1 required for conveying the yellow sand substrate is given by

$$A_1 = \left(\frac{(H-h)^2}{H^2}\right)A \tag{7}$$

where A_1 is the actual cross-sectional area required for yellow sand substrate transportation, mm^2; h is the tillage depth, mm.

The minimum soil delivery rate is expressed as

$$Q_{min} = \rho V_m A_1 \tag{8}$$

where Q_{min} is the minimum throughput, kg/s; V_m is the average material conveying speed, m·s^{-1}.

Substituting Equations (6) and (7) into Equation (8) yields

$$Q_{min} = \rho V_m \frac{(H-h)^2}{H^2} \frac{(L_1 + L_2)H}{2} \tag{9}$$

In practical ridging operations, the working process of the ridger resembles that of an open-type screw conveyor transporting material toward the center, thus:

$$Q_1 \geq \frac{Q_{min}}{2} \tag{10}$$

To meet the above ridge profile requirements, the ridger must satisfy the condition that the actual soil delivery rate exceeds the required rate. Substituting Equations (5) and (9) into Equation (10) gives the constraint for the yellow sand substrate throughput as

$$47\mu D^2 Sn\rho\sigma = \rho V_m \left(\frac{(H-h)^2}{H^2}\right)\left(\frac{(L_1 + L_2)H}{2}\right) \tag{11}$$

2.3.3. Variable-Pitch Design of the Helical Ridging Blade

The ridging blades L of the ridger are arranged along the shaft of the rotary tillage mechanism. The blades are distributed helically along the shaft, and the spiral ridging blades utilize the preceding section of the screw to break and convey the substrate. By integrating spiral motion with mechanical design, the combined action of the preceding and trailing screw segments effectively compacts and forms the ridge. Based on the motion characteristics of the yellow sand substrate and its specific working requirements, the variable-pitch design of the spiral ridging blades is proposed, as shown in Figure 4a.
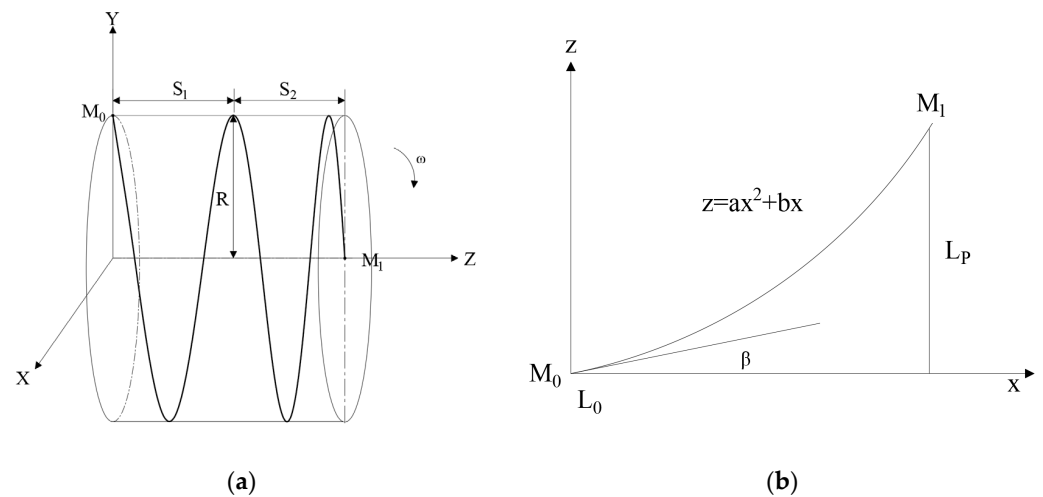
Figure 4. Variable-pitch helical curve of the ridging blade: (**a**) Schematic of the variable-pitch helical geometry; (**b**) Development diagram of the variable-pitch helical curve.

When point M moves along the Z-axis with uniform angular velocity ω, the helical trajectory of the blade changes with the pitch, producing a variable-pitch helical curve. In this motion, point M performs a uniform circular motion around the shaft while simultaneously executing translational motion along the Z-axis.

Based on this kinematic principle, the Z-axis is taken as the axis of the ridging blade, and a Cartesian coordinate system is established as illustrated in Figure 4b. Let R be the helix radius, M_0 the starting point of the spiral, and β the initial helix angle. When point M moves along the helix, the axial displacement is denoted L_p. The parametric equation of the helical curve in terms of R, β, k, L_p, can be expressed as

$$Z = ax^2 + bx \tag{12}$$

where a and b are coefficients of the curve.

If β_k represents the helical rise angle at any point on the blade, the slope of the tangent to the helical curve at that point is given by

$$\frac{dz}{dx} = tan\beta_k = ax + b \tag{13}$$

When $x = 0$, $\beta_k = \beta_0$:

$$b = tan\beta_0 \tag{14}$$

When $Z = L_p$, $x = 2\pi Rk$:

$$a = \frac{L_p - 2\pi Rktan\beta}{(2\pi Rk)^2} \tag{15}$$

Substituting Equations (14) and (15) into Equation (12) yields the helical line equation:

$$Z = a(2\pi Rk)^2 + 2\pi Rktan\beta \tag{16}$$

The variable *k* represents the number of helix turns, and its value can be greater than 1; however, in the Cartesian coordinate system, the parameter t used in the equation must not exceed 1. Owing to the difference in their definitions, the equation requires further modification. The relationship between *k* and t is expressed as

$$k = \frac{\omega}{2\pi}t \tag{17}$$

Accordingly, the designed variable-pitch helical blade surface can be expressed as

$$\begin{cases} x = Rcos(2\pi k) \\ y = Rsin(2\pi k) \\ z = a(2\pi Rk)^2 + 2\pi Rk tan\beta \end{cases} \tag{18}$$

The ridging blades are arranged in a variable-pitch helical configuration, with the mounting angle γ of each blade holder maintained between 25° and 26°. Within the same rotational plane, the rotary–ridging composite blade drum adopts a symmetrical arrangement on both the left and right sides to ensure that the blades on either side enter the soil simultaneously. This configuration balances the lateral forces of the ridge-forming and film-mulching machine, enabling it to travel in a straight path without deviation.

The spacing between adjacent rotary tillage blades is set greater than the working width of a single blade, thereby preventing unworked gaps between axially adjacent blades. On the right side, six blades are evenly distributed along the helical line, with adjacent angular positions of 150°. The corresponding installation positions are shown in Figure 5 as $z_1 = 20$ mm, $z_2 = 100$ mm, $z_3 = 170$ mm, $z_4 = 230$ mm, $z_5 = 280$ mm, $z_6 = 330$ mm. The blades on the left side are mounted symmetrically to those on the right.
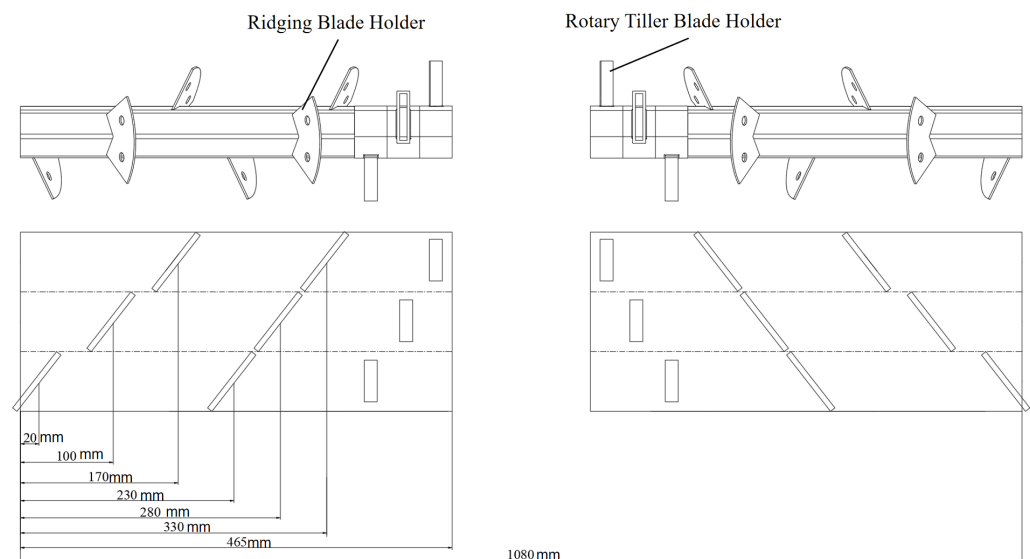

Figure 5. Unfolded layout of the rotary–ridging blade arrangement.

2.3.4. Shaping System

The shaping unit is positioned at the center of the machine and functions to deliver the loosened yellow sand substrate, processed by the rotary tillage mechanism, into a predefined rectangular space according to the agronomic ridge profile requirements. By applying compaction, it forms a trapezoidal ridge, thus completing the ridge-forming process.

A single fixed ridge profile limits the operational scope of the machine. Through the integration of modular design and an innovative adjustment mechanism, the ridge-forming and film-mulching machine overcomes the constraints of conventional equipment with fixed ridge parameters, achieving adjustable ridge height and width. This enables flexible adaptation of the ridge profile to meet varying crop cultivation requirements or complex terrain conditions, without the need for component replacement. By enabling on-demand ridge dimension adjustment, the mechanism greatly improves the equipment's operational flexibility and adaptability in yellow sand substrate environments. It also offers a highly compatible technical solution for precision agricultural management and a variety of planting patterns, as depicted in Figure 6.
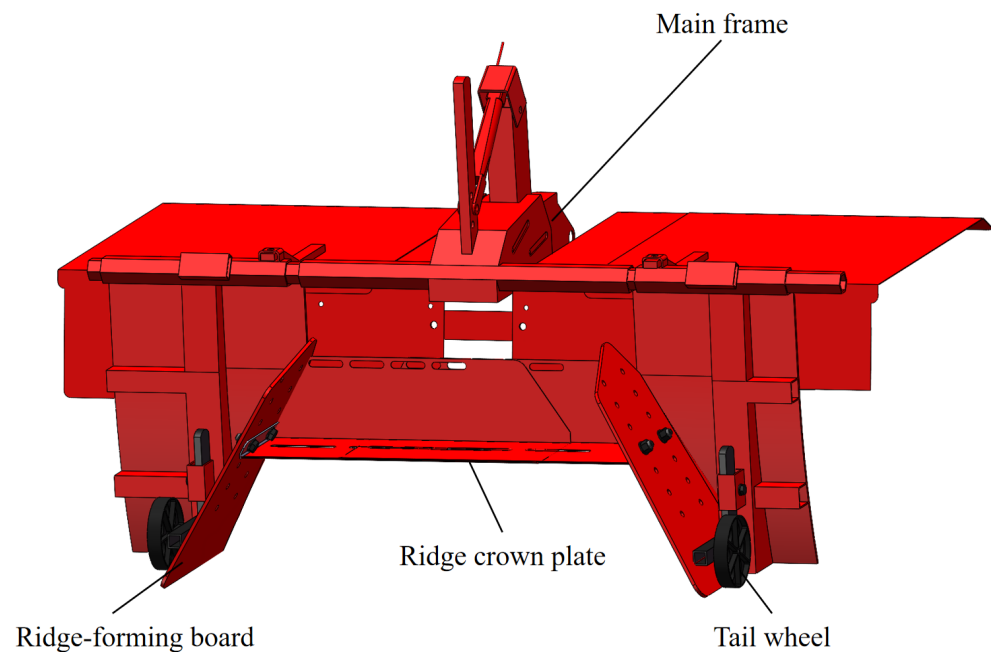
Figure 6. Structural schematic of the ridge-shaping system.

During operation, the ridge shape is determined by the external parameters of the shaping mechanism. To ensure compaction and accurate formation in a single pass, the working face of the shaping mechanism must match the target ridge profile. According to the ridge-forming requirements specified for tomato cultivation, the shaping mechanism is designed with the following dimensions: ridge height $H = 200$ mm, top width $B_1 = 600$ mm, and base width $B_2 = 800$ mm.

The left and right ridge boards and two top plates for producing the ridge crest make up the ridge-forming assembly. For instance, the left ridge board has two side baffles and a rear baffle. While the right side baffle is welded to the rear baffle at a particular inclined angle, the rear baffle and the left side baffle are welded together at a right angle (90°). The top plates and side ridge boards can be fully adjusted.

2.3.5. Film-Mulching Mechanism

In the design of the equipment, this study focuses on the force transmission path of the mulching device and its interaction with the film-soil interface. Through rational structural optimization and parameter adjustment, the operating parameters of the mulching device can significantly improve the uniformity of the force distribution and friction transfer within the soil-film contact zone. Considering that soil self-friction is insufficient to ensure mulching quality in low-friction environments, this study introduces a rotatable slider structure to optimize the pressure transmission path and enhance the interface friction. Additionally, a spring-loaded pressing wheel structure is incorporated at the edge of the film to improve the anchoring force and wind resistance of the film.

The design objective of the mulching mechanism is to evenly lay the film on the yellow sand substrate. Addressing the limitations of traditional mulching machines that lack elasticity, this design utilizes an adjustable-width, adjustable-suspension top-clip mulching device. The rotational slider mechanism ensures the smooth laying of the film. During operation, one side of the film is fixed onto the film rack by spring pressure, with the other side similarly installed. As the machine advances, the film rotates and extends on the film rack, completing the mulching process. This device is compatible with commercially available films ranging from 800 to 1200 mm in width, with spring-loaded collars on both sides to prevent lateral movement, facilitating both installation and disassembly. After

the ridging operation is completed, the film extends from the film rack, and the pressing roller compresses the film onto the ridge surface with its own weight. The rear pressing wheel further consolidates the edges of the film. A spring-loaded pressing wheel structure is added at the edge of the film, enabling self-adaptive adjustment of the pressing force through the spring's elastic action. This structure not only provides consistent downward pressure during mulching but also automatically adjusts the pressing force in response to variations in soil surface topography and substrate looseness, ensuring proper film-substrate adhesion. Finally, the soil-covering wheel places yellow sand substrate over the tightly pressed film edges, completing the entire mulching process.

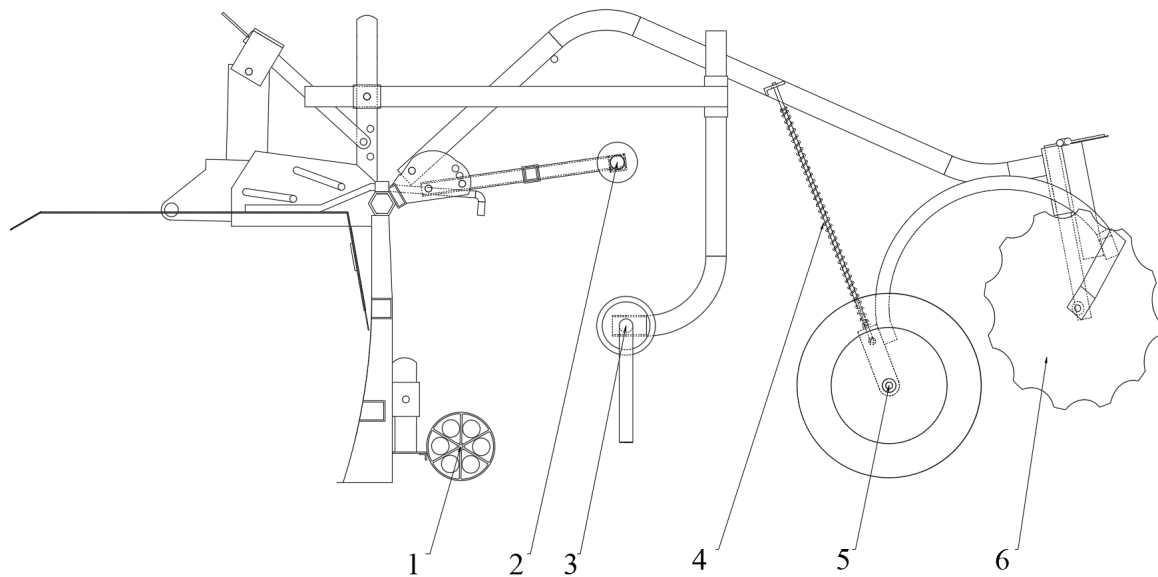A schematic of the mulching mechanism is shown in Figure 7:

Figure 7. Structural schematic of the mulching device. 1 walking wheel; 2 mulch rack; 3 pressing roller; 4 spring; 5 pressing wheel; 6 soil-covering disc.

When the mulch is fed by the hanging device, the roll of mulch suspended on the rack is pulled out by the tensile force generated by the pressing unit. The relative installation position of the mulch roll and the pressing roller affects the stress state of the film, thereby influencing the mulching quality [31]. As shown in Figure 8, when the pressing roller exerts a pulling force F on the mulch, the pulled section of the film forms an angle α with the horizontal ground. Different relative positions between the hanging device and the pressing roller result in different α values ($\alpha_1 > \alpha_2$).

For a constant pulling speed and equal roll radii ($R_1 = R_2$), the tensile force applied to the film is identical ($F_1 = F_2$). The horizontal component of the force is $F_x = F_{\cos\alpha}$, and the vertical component is $F_y = F_{\sin\alpha}$. Given that $\alpha_1 > \alpha_2$, it follows that $F_{x1} < F_{x2}$ and $F_{y1} > F_{y2}$. Since the horizontal distance between the hanging device and the pressing unit is much smaller than the vertical distance, the mulch experiences a relatively small horizontal force and a relatively large vertical force.

To prevent film breakage during pulling, it is necessary to analyze the magnitude of the vertical component F_y. According to the literature, the traction force required to pull out the mulch roll is approximately 2.199 N, and the maximum α_1 value is 90°. Calculations show that the maximum stress on the film is about 0.14 MPa, which is far below its tensile strength. Therefore, the relative installation angle between the hanging device and the pressing roller can be adjusted within 90° without damaging the film. The optimal relative position must be determined based on the effect of the pressing roller's working position on mulching quality.
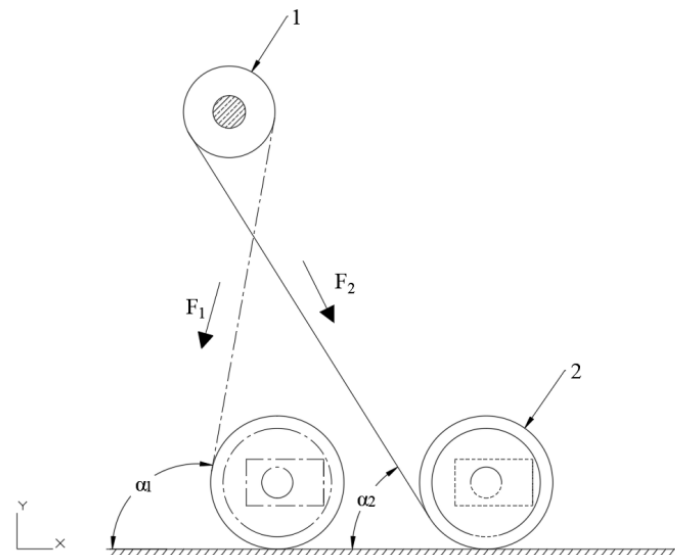
Figure 8. Analysis of the positioning of the plastic film during mulching operation: 1 plastic film roll; 2 pressing roller.

When the pressing unit is in operation, the force analysis of the pressing roller is shown in Figure 9. The most significant factors affecting mulching quality are the load W (external load and self-weight) applied by the pressing roller to the soil–film interface and the penetration depth H_1 [32]. These parameters must be effectively controlled to ensure consistent quality. When the pressing roller rotates under the driving force F, the soil and the mulch exert a compressive reaction force dF on the small contact arc segment s at point B of the ABC contact region. This can be expressed as

$$dF = PBdS \tag{19}$$

where P is the compressive strength of the yellow sand substrate, MPa; B is the width of the mulch pressing roller, mm.
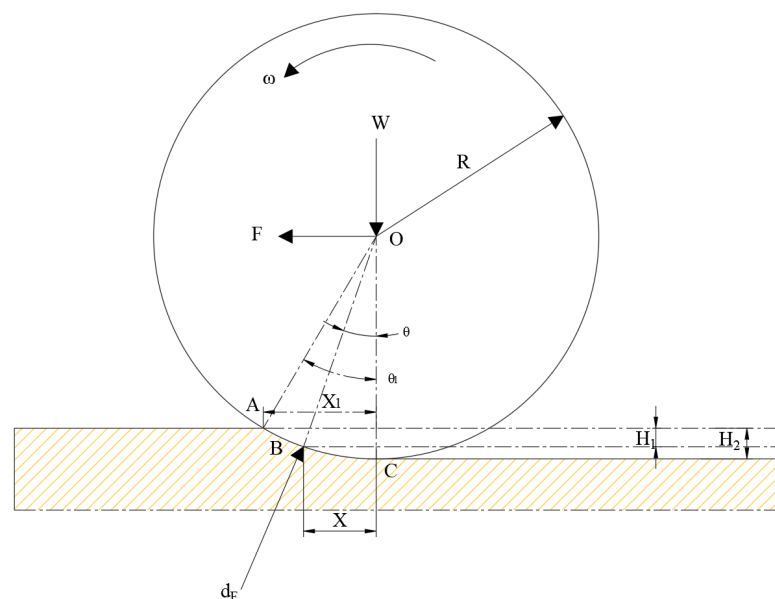

Figure 9. Force analysis of the mulch pressing roller. The yellow area represents the soil beneath the roller, which is subjected to pressure during the rolling process. A is the point where the roller contacts the soil surface, B is the point where the force vector F intersects the soil surface, and C is the point where the force F is applied to the soil at a certain distance X.

Since the load applied to the pressing roller is equal in magnitude to the total compressive reaction force dF exerted by the soil–film interface, it follows that

$$W = \int \mathrm{dF}\cos\theta = B\int P\cos\theta \,\mathrm{dS} \tag{20}$$

For the small arc segment s corresponding to point B, the infinitesimal displacement along the x-direction is dx, thus dS = cos θ dx. Accordingly, the total load over the ABC contact surface can be expressed as

$$W = B\int_0^{x_1} P\mathrm{dx} \tag{21}$$

Based on Bekker's classical theory, the relationship between the compressive strength P of the yellow sand substrate and the penetration depth H_1 can be described by the following empirical expression:

$$P = kH_1^n \tag{22}$$

where k is the composite modulus of deformation of the yellow sand substrate; n is the nonlinear compression index of the yellow sand substrate.

$$k = \frac{k_c}{B}k_\varphi \tag{23}$$

where k_c is the cohesive component of the yellow sand substrate; k_φ is the frictional component of the yellow sand substrate.

$$R_c = \frac{BkH_0^{(n+1)}}{(n+1)} \tag{24}$$

$$H_0^{(n+\frac{1}{2})} = \frac{3W}{Bk\sqrt{D}(3-n)} \tag{25}$$

Within the theoretical framework defined by Equations (19)–(25), the penetration depth of the mulch pressing roller is governed by the coupled influence of mechanical structural parameters, the physical properties of the yellow sand substrate, and operational conditions. Specifically, the roller width B, radius R, and vertical load W directly determine the penetration depth through geometric constraints and mechanical equilibrium. The substrate's modulus of deformation k and compression index n regulate the threshold of penetration via the nonlinear material response, while the kinematic effect of the forward velocity v introduces rate sensitivity into the system. Theoretical analysis indicates that the penetration depth H_1 exhibits a negative correlation with the forward velocity, with a power-law relationship revealing the physical mechanism by which higher operating speeds suppress substrate compression. Conversely, the positive correlation with vertical load reflects the enhancement of plastic deformation in the yellow sand substrate under increased loading. The interaction between substrate parameters and mechanical parameters is manifested through dimensionally integrated terms; however, the precise coupling relationships require further calibration through experimental validation.

In actual operations, the dynamic contact interface between the mulching roller and the yellow sand substrate is affected by time-varying boundary conditions, such as initial subsidence disturbances and rheological properties of the yellow sand, leading to significant uncertainties in mechanical responses. This manifests in the uneven distribution of contact pressure and the lag effect in dynamic responses. To improve the prediction accuracy of the model, field tests under multiple conditions should be conducted to systematically quantify the multi-parameter coupling characteristics of the yellow sand substrate, and

a three-dimensional contact mechanics model with viscoelastic constitutive relationships should be introduced to enhance the accuracy of simulating the mechanical behavior.

Building on existing research, it is evident that low-cohesion sandy substrates exhibit insufficient friction at the film-soil interface, often leading to limited membrane tension. Consequently, structural optimization is required to compensate for this limitation. Previous studies have highlighted the critical role of the frictional properties of the film material in determining tension transmission, and experiments have confirmed the limited level of membrane-soil interface forces in sandy soils from southern Xinjiang [33]. Additionally, controlling operational parameters can effectively improve the force distribution and friction transmission at the membrane-soil interface [34]. Furthermore, optimizing the soil-covering structure has been proven to significantly enhance the anchoring of the membrane edges, improving wind resistance and mulching stability. Based on these findings, this study introduces an innovative design featuring a rotatable slider structure and secondary compaction unit to optimize the downward pressure transmission path and enhance the film tension and conformity. This solution, proposed for the low-friction yellow sand substrate, is not only reasonable but also holds substantial application potential, providing new design ideas and technical references for mechanized mulching.

2.4. Simulation of the Ridging Operation Process of the Ridge-Forming and Film-Mulching

The ridging operation of the ridge-forming and film-mulching machine was simulated using EDEM 2020 software to compare the performance of constant-pitch and variable-pitch helical ridging blades. The simulation comprehensively evaluated the effects of forward speed, blade shaft rotational speed, and penetration depth on ridge profile stability and power consumption. The results demonstrated that the variable-pitch helical blade outperformed the constant-pitch design in both ridge uniformity and energy efficiency. Based on the simulation findings, the optimal operating parameters were determined, providing a robust reference for the design and parameterization of the machine.

2.4.1. Parameter Configuration

In the discrete element modeling (DEM) of the sandy substrate, accurate specification of the substrate's material parameters is critical for ensuring the reliability of simulation results. In this study, the particle characteristics of the sandy substrate were determined based on field sampling from a solar greenhouse in Shuangcheng Town, Alar City, Xinjiang. Combining physical calibration tests with published literature, the contact parameters of the sandy substrate particles were established, enabling the development of an applicable DEM model for the substrate. The detailed parameter settings are presented in Table 2.

Table 2. Parameter settings for the DEM simulation.

Item	Unit	Value
Sandy substrate length $\times$ width $\times$ height	mm^3	$2000 \times 1200 \times 300$
Forward speed	m·s^{-1}	0.4–0.6
Blade shaft rotational speed	rpm	240–260
Penetration depth	mm	140–160
Sandy substrate density	kg/m^3	1405
Sandy substrate Poisson's ratio		0.35
Sandy substrate shear modulus	Pa	1×10^6
Steel density	kg/m^3	7860
Steel Poisson's ratio		0.4
Steel shear modulus	Pa	8×10^{10}
Critical normal stress	KPa	50
Critical tangential stress	KPa	30

2.4.2. Sandy Substrate Particle Model Construction

To establish a DEM simulation model that closely reflects real tillage conditions, typical physical parameter tests were conducted on the yellow sand substrate collected from a solar greenhouse at the Sixth Regiment in Alar City, Xinjiang. The bulk density was first measured using a bulk density tester, yielding a value of 1405 kg/m^3 (see Figure 10). The procedure involved allowing the dried substrate to fall freely through a funnel into a graduated cylinder, leveling the surface, and then weighing it to calculate density as the mass-to-volume ratio. This measurement was repeated five times, and the mean value was taken. The primary aim of this study was to apply well-established DEM modeling techniques to the specific working conditions of the yellow sand substrate for machinery optimization; therefore, parameter acquisition followed standard calibration methods, with a particular emphasis on verifying the validity of the model.
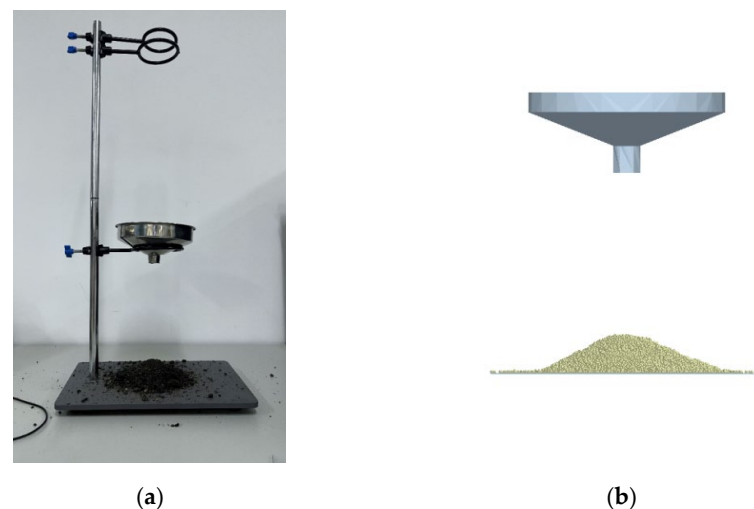

(**a**)   (**b**)

Figure 10. Measurement and DEM simulation of the angle of repose of the yellow sand substrate. (**a**) Experimental setup for angle of repose measurement; (**b**) DEM simulation in EDEM reconstructing particle piling and repose angle (average angle of repose = 34.85°).

Subsequently, the angle of repose was measured using an apparatus consisting of an iron stand, funnel, measuring cylinder, electronic balance, and digital inclinometer. The yellow sand substrate was allowed to fall freely under gravity to form a conical pile, and image processing techniques were employed to calculate an average angle of repose of 34.85°. On this basis, typical contact parameters for soil discrete element models reported in the literature [35,36] were adopted, with reference to previous studies that experimentally calibrated the bonding parameters of moist sandy soils. The results indicated that in a 5:3 sand–slag mixture with a moisture content of approximately 11%, the apparent macroscopic cohesion was very small, about 2–3 kPa [17,25]. This implies that only a very low bond strength between particles is required to reproduce such a weakly cohesive state. Accordingly, the bond strength in the model was set to a relatively low range, ensuring that the simulated repose angle and loose packing characteristics approximated those of cohesionless dry sand, but with slight cohesion that enabled the heap to maintain its shape while collapsing under minor disturbance. In this way, a particle contact mechanics parameter system suitable for this type of substrate was established (see Table 3).

This study innovatively mixed yellow sand and slag in a 5:3 mass ratio, creating a loose, highly permeable substrate structure and modeling its dynamic behavior during tillage. This 5:3 sand–slag ratio has been widely adopted in local facility cultivation practices due to its practical adaptability [6]. Existing research and preliminary experimental results show significant differences in the physical properties of the substrate and its impact on

operational performance under varying sand–slag ratios [37]. Specifically, increasing the slag proportion causes the substrate structure to become looser, significantly improving porosity and permeability, but at the same time, ridge stability decreases, with a higher risk of top collapse and side slope sliding. In contrast, increasing the sand ratio enhances compressive strength and ridge stability, but permeability and aeration decrease, which could negatively affect root growth.

Table 3. The contact mechanics parameters for the sandy substrate particles.

Parameter Type	Restitution Coefficient	Static Friction Coefficient	Rolling Friction Coefficient
Sandy substrate–sandy substrate	0.45	0.7	0.03
Sandy substrate–65Mn steel	0.35	0.45	0.25

Therefore, the 5:3 sand–slag ratio is widely used in local practices, as it balances ridge stability with good permeability and aeration, while also ensuring the feasibility of mechanized operations and meeting crop cultivation needs. However, this study recognizes that different ratios may affect the ridging and mulching performance, and this issue will be further explored in subsequent comparative experiments.

Based on field samples collected from solar greenhouses, microscopic image analysis revealed that the substrate particles are predominantly spherical or plate-shaped, with clear boundaries and regular shapes (see Figure 11). Consequently, spherical particles and multi-sphere aggregates were used in geometric modeling in EDEM to better simulate their motion trajectories and contact responses under mechanical disturbance, thus laying the foundation for subsequent discrete element analysis of ridging and mulching operations [38].
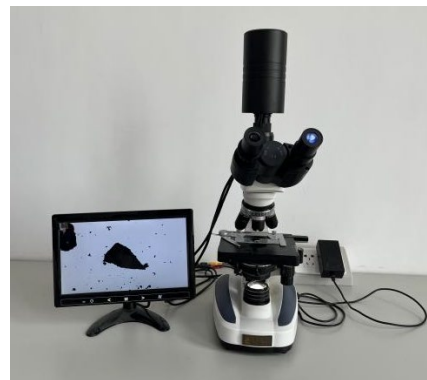

Figure 11. Optical microscope image of the particle size analyzer. The system consists of a digital microscope and an image acquisition module, enabling direct observation and measurement of particle morphology and equivalent size distribution. Image processing was applied to extract parameters such as aspect ratio and sphericity, providing key input for DEM particle modeling and parameter calibration.

The particle size distribution of the yellow sand substrate was determined through a standard sieving experiment. The instruments used included a ZBSX-92A vibrating sieve shaker and an electronic balance. Particle size analysis revealed that the cumulative percentage of particles larger than 0.6 mm accounted for approximately 71% of the total, while those larger than 0.2 mm accounted for about 96% (see Table 4). This result indicates that the yellow sand substrate exhibits a relatively wide particle size gradation. However, it should be noted that the numerical model did not fully capture this distributional variability in the particle size settings, which constitutes one of the main discrepancies between the simulation results and actual conditions.

Table 4. Particle size distribution of the sandy substrate.

Particle Grade	Particle Size/mm	Percentage/%	Cumulative Percentage/%
Gravel	>2	37	37
Coarse sand	0.6–2	34	71
Medium sand	0.2–0.6	25	96
Fine particles	<0.2	4	100

To improve computational efficiency, and following previous studies [17,25,31], the simulation particle size was set to 5 mm. In the EDEM software, a single-sphere model with a radius of 5 mm was employed to represent the basic yellow sand particles, thereby achieving a balance between computational complexity and physical accuracy. In the EDEM software, a monodisperse spherical element with a radius of 5 mm was employed to represent the substrate particles. Based on the morphological characteristics of the physical material, a four-sphere clumping method (sphere radius r = 5 mm) was adopted to capture the irregular geometry of gravel aggregates. The particle–particle contact radius was set to 4.5 mm.

The contact interactions were modeled using the Hertz–Mindlin contact theory, which captures the nonlinear force–displacement relationship during collisions. The spatial arrangement of the spheres was adjusted to achieve volumetric equivalence with the actual aggregates, maintaining a deviation below 3.5%. Energy dissipation during collisions was accounted for via the Hertz–Mindlin nonlinear contact model.

All simulation parameters were calibrated against laboratory measurements and literature benchmarks to ensure consistency between the simulated packing behavior and the mechanical response of the substrate. This modeling strategy balances physical fidelity with numerical stability and computational efficiency. The final simulated particle assembly of the sandy substrate is illustrated in Figure 12.
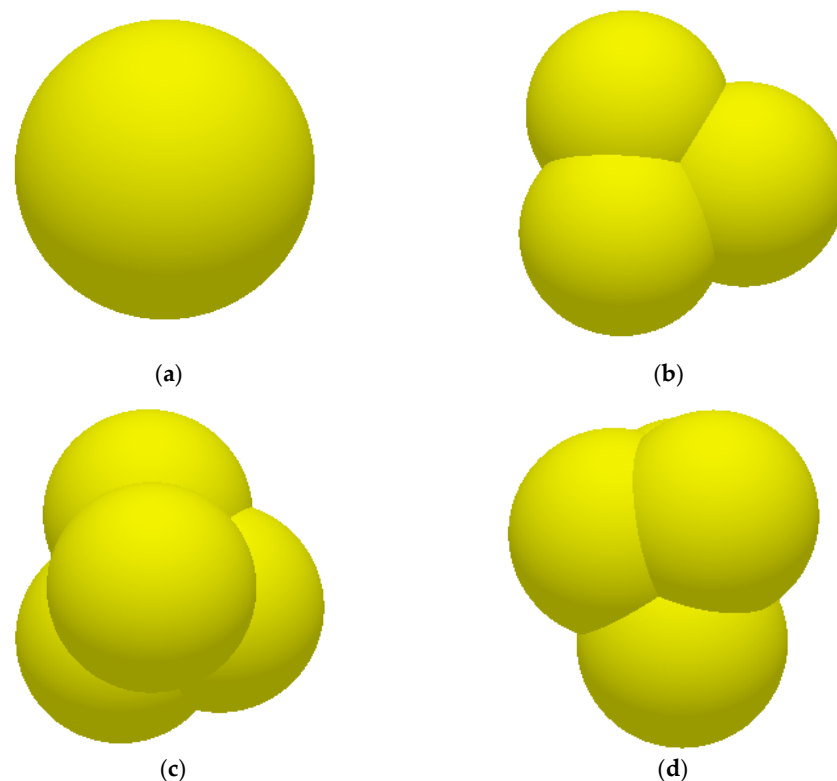

(a)

(b)

(c)

(d)

Figure 12. Schematic of the particle model: (**a**) single-sphere element (radius 5 mm) representing yellow sand particles, balancing computational efficiency and physical accuracy; (**b**) four-sphere clump model on the X-axis plane, approximating the irregular geometry of slag particles to better capture bulk den-

sity and contact behavior; (**c**) four-sphere clump model on the Y-axis plane, showing the arrangement of the spheres from a different perspective; (**d**) four-sphere clump model on the Z-axis plane, representing another view of the clump configuration to ensure realistic reproduction of the repose pile.

The dimensions of the discrete element method (DEM) soil bin model were set to 2000 mm × 1400 mm × 300 mm (length × width × height), containing a total of approximately 470,000 particles. Based on material mechanics test data, the physical parameters of the system were determined (Tables 2 and 3). The contact interactions between sandy substrate particles were modeled using the Hertz–Mindlin with Bonding model, in which bond keys simulate the cohesive forces between particles. Adjacent particles were bonded through cohesive forces capable of withstanding both tangential and normal displacements; bond breakage occurred when the maximum shear stress threshold was exceeded, resulting in particle fragmentation. The soil-crushing performance of the rotary tillage system was quantitatively evaluated by counting the number of broken bonds. Contact interactions between the sandy substrate and the tillage components were modeled using the Hertz–Mindlin (no-slip) model.

In the EDEM simulation, sandy substrate particles were generated via the particle factory module. A static filling mode was applied to uniformly distribute particles within the simulation domain, followed by a 0.5 s dynamic relaxation period to allow particles to fully settle under gravity until a stable configuration was reached. Particle stability was verified by monitoring the decay of their motion velocity. Subsequently, the geometric model of the tillage components was imported to construct the coupled sandy substrate–machinery interaction system. Simulation parameter settings strictly adhered to the grid size criterion (element size to particle diameter ratio = 2:1) and the Rayleigh time-step theory, ensuring a balance between numerical convergence and computational efficiency (see Figure 13).
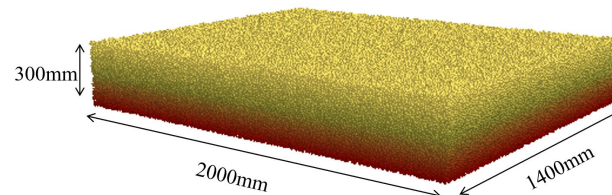

Figure 13. Simulated soil-bin model of the yellow sand substrate used for discrete element analysis.

2.4.3. Establishment of the Simulation

To reduce computational complexity and improve simulation efficiency, the full machine model was simplified: all rigidly connected components of the implement were merged into a single entity, and the rotary tiller drum assembly was integrated into a unified module to accurately reproduce the soil–tool interaction dynamics (see Figure 14). The numerical solution time step was set to 1.73×10^{-5} s, with a mesh size of 10 mm and a data recording interval of 0.1 s, ensuring both high computational accuracy and efficient use of computational resources.
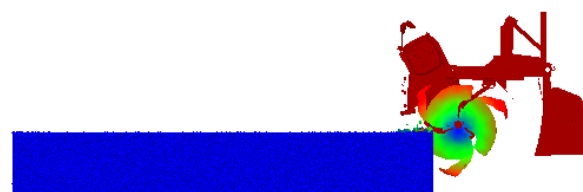

Figure 14. Schemes follow the same formatting. The rotary tiller, ridging blades, gearbox, and shaping plates were imported into the stabilized soil bin in STEP geometry format. This simulation framework enables quantitative evaluation of soil disturbance and ridge morphology under different

operating parameters. The colors represent the soil disturbance intensity: blue indicates regions with low disturbance (soil), green and yellow represent moderate disturbance, red indicates areas with high disturbance, and dark red represents the shaping plates of the machine.

2.4.4. Simulation Test Design

Based on the discrete element soil tank simulation, this study systematically evaluated the operational performance of the rotary–ridging blade drum in a yellow-sand substrate. In accordance with the operational requirements of the ridging and mulching process (see Figure 15), three key factors were selected: tillage depth (A), blade shaft rotational speed (B), and forward travel speed (C). Two performance indices were adopted—ridge height qualification rate (Y_1) and light-receiving surface width qualification rate (Y_2). A three-factor, three-level orthogonal experimental design was employed. Variance analysis and range analysis were conducted to identify the optimal parameter combination, providing a theoretical basis for optimizing ridging quality.
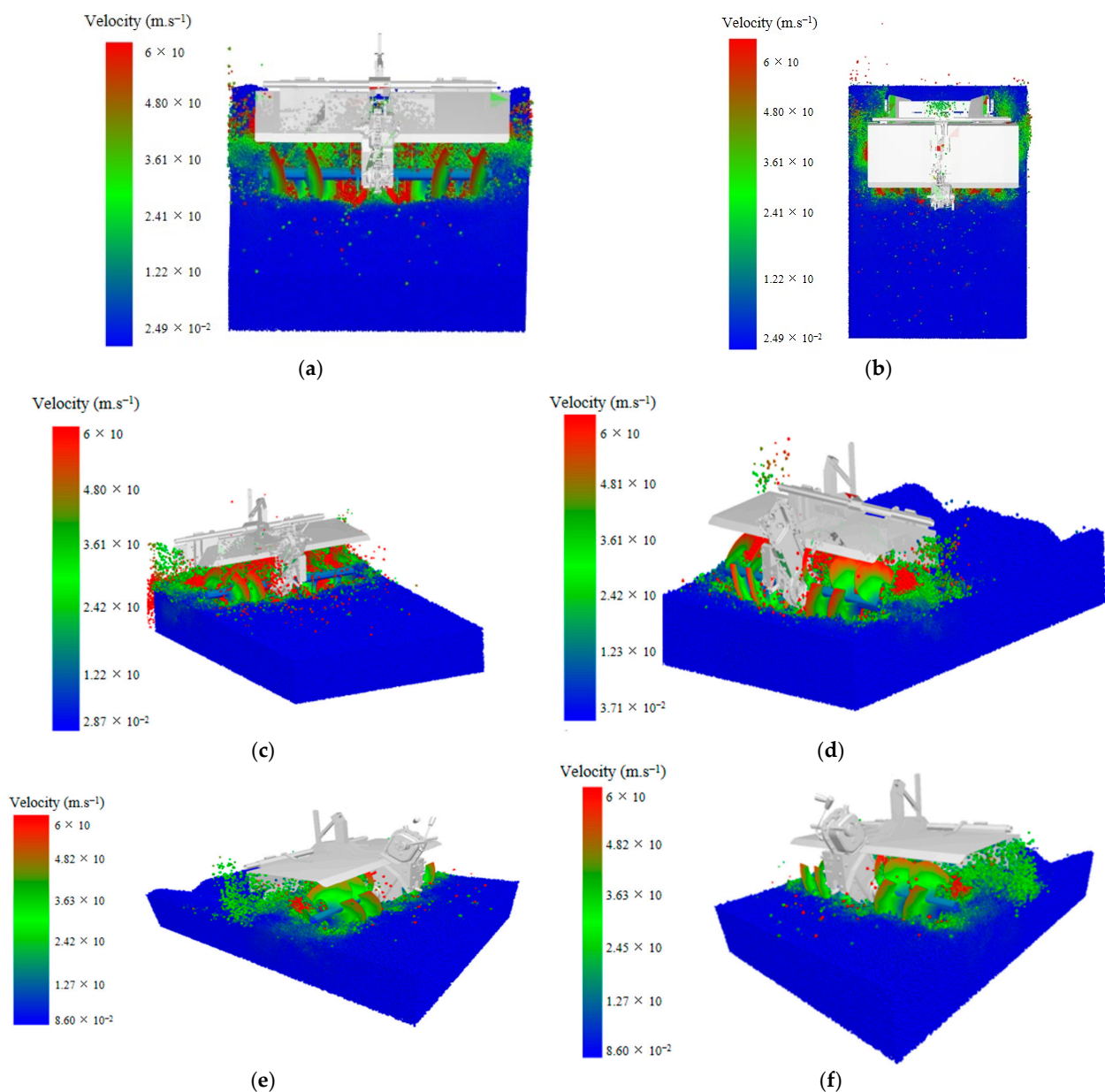
(a)

(b)

(c)

(d)

(e)

(f)

Figure 15. *Cont.*
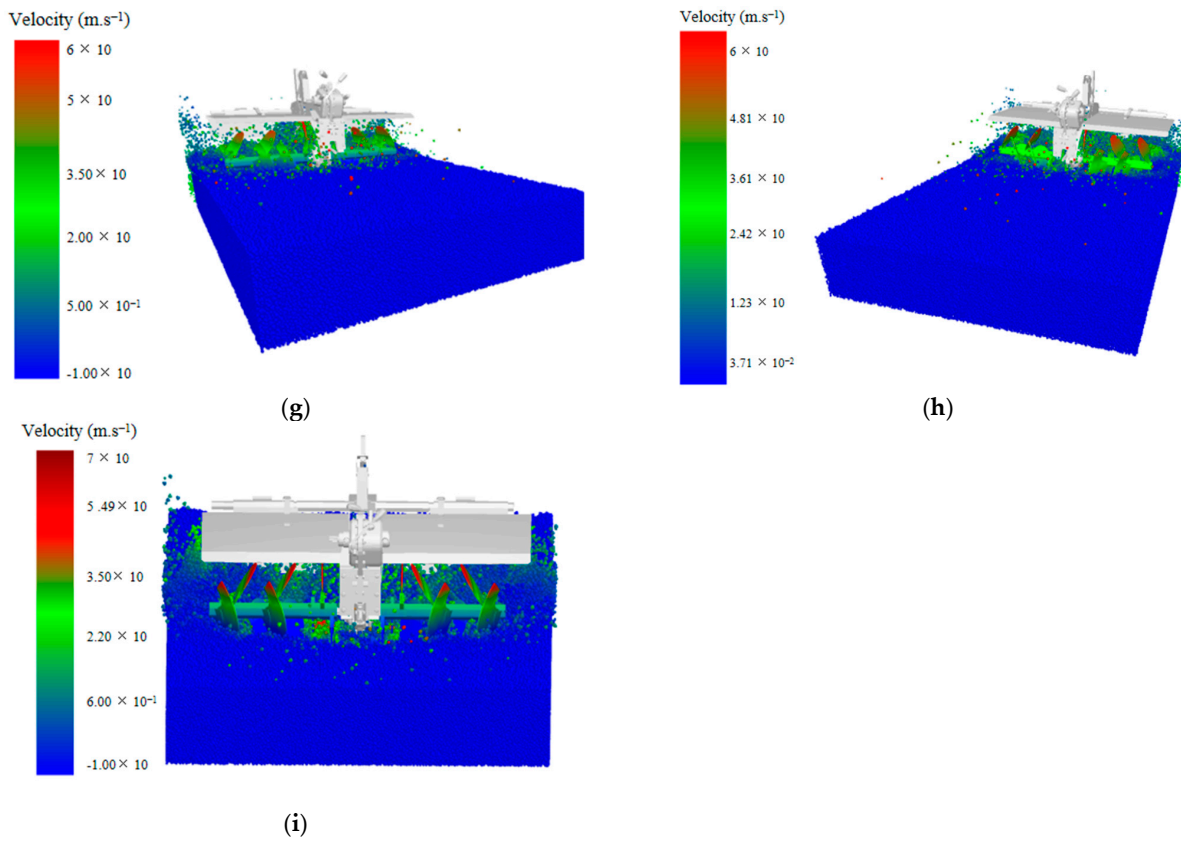
(**g**)

(**h**)

(**i**)

Figure 15. Simulation test design: Simulation of the ridging–mulching machine under different operating conditions. The simulations illustrate the influence of various operating parameters on soil particle dynamics and ridge stability. Soil particle velocity. Notes: (**a**) forward speed $v = 0.6$ m·s^{-1}, blade shaft speed n = 240 rpm, tillage depth 150 mm; (**b**) $v = 0.6$ m·s^{-1}, n = 250 rpm, tillage depth 150 mm; (**c**) v = 0.6 m·s^{-1}, n = 260 rpm, tillage depth 150 mm; (**d**) v = 0.8 m·s^{-1}, n = 240 rpm, tillage depth 150 mm; (**e**) v = 0.8 m·s^{-1}, n = 250 rpm, tillage depth 150 mm; (**f**) v = 0.8 m·s^{-1}, n = 260 rpm, tillage depth 150 mm; (**g**) v = 1 m·s^{-1}, n = 240 rpm, tillage depth 150 mm; (**h**) v = 1 m·s^{-1}, n = 250 rpm, tillage depth 150 mm; (**i**) v = 1 m·s^{-1}, n = 260 rpm, tillage depth 150 mm.

2.5. Traction and Energy Metrics

To ensure the traceability and reproducibility of the traction and energy consumption statements, this study defines a unified system for the measurement and symbols of traction force, drawbar power, area-normalized drawbar energy, and specific draft [39]. The distinction is made between tool-level and system-level energy consumption. The drawbar power is defined as

$$P_{DB} = Fv = \frac{FS}{3.6} \qquad (26)$$

where F represents the traction force, v is the travel speed (m·s^{-1}), and S is the travel speed in km·h^{-1}. The area-normalized drawbar energy (MJ·ha^{-1}) is calculated by integrating the drawbar power over time (or traction force over displacement) and normalizing it by the effective working area:

$$E_{DB} = 0.01 \frac{\overline{F}}{w} \qquad (27)$$

where W is the effective working width (m), and $\overline{F}$ is the steady-state, distance-weighted average traction force (N). In the engineering management context, the drawbar energy (E_{DB}) can also be estimated using the drawbar power and effective field capacity (EFC, ha·h^{-1}):

$$EFC = \frac{S \cdot W \cdot FE}{10} \qquad (28)$$

where S is the travel speed (km·h^{-1}), W is the working width (m), FE is the field efficiency (usually $0 < FE \leq 1$).

To eliminate the influence of width and depth, specific draft is defined as

$$SD = \frac{F}{Wd} \tag{29}$$

where SD is the specific draft (kPa), F is the traction force (N), W is the working width (m), d is the tillage depth (m).

System-level energy is defined as the total area-normalized energy required to complete the same agronomic task across all operations:

$$E_{seq} = \sum_{k=1}^{N} E_{DB,K} \tag{30}$$

where E_{seq} is the system-level energy, the total energy required to complete the entire operation sequence (MJ·ha^{-1}), N is the number of passes required for the operation, $E_{DB,k}$ is the area-normalized drawbar energy for the k-th operation in the sequence (MJ·ha^{-1}).

When traction force sensors are not installed, the energy consumption can be estimated using the power and effective field capacity (EFC) as follows:

$$E_{DB} = \frac{3.6 \cdot \overline{P}_{DB}}{EFC} \tag{31}$$

where $\overline{P}_{DB}$ is the average drawbar power (kW), EFC is the effective field capacity (ha·h^{-1}).

If direct traction measurements are unavailable, engine power and operational efficiency (EFC) can be used to estimate energy consumption.

2.6. Greenhouse Ridge–Mulching Field Experiment Design

Experimental Conditions and Materials

In October 2024, a field experiment was conducted in the experimental plots of the 7th Company, Shuangcheng Town, 6th Regiment, Alar City, First Division of the Xinjiang Production and Construction Corps (see Figure 16), to evaluate the performance of the ridge–mulching machine. The experimental field consisted of a yellow-sand substrate, and all conditions were maintained uniformly throughout the test period. During the trials, the ambient temperature was approximately 22 °C, with a relative humidity of 46%. Using the five-point sampling method, the firmness and moisture content of the yellow-sand substrate were measured at depths of 10 cm, 20 cm, and 30 cm. The results were as follows: at 10 cm depth, mean firmness was 113.4 kPa with a moisture content of 11.0%; at 20 cm depth, mean firmness was 135.4 kPa with a moisture content of 11.3%; and at 30 cm depth, mean firmness was 155.3 kPa with a moisture content of 11.4%. During the experiment, due to the differences in evaporation between the soil surface and deeper layers in the greenhouse, the moisture content of the substrate fluctuated between 11.0% and 11.4% at depths of 10 cm to 30 cm. This fluctuation is considered normal, and we have controlled the initial moisture content and ensured its uniform distribution, so the impact of this fluctuation on the experimental results can be neglected. The equipment used in the experiment included the ridge–mulching machine, a digital soil compaction tester, a soil moisture meter, a steel tape measure, a steel ruler, and an electronic balance.

Figure 16. Field testing of the ridge–mulching machine. The arrow indicates the forward direction of the machine.

3. Results and Discussion

3.1. Analysis of Simulation Results

3.1.1. Simulated Ridge Profile

In this study, the Discrete Element Method (DEM) was employed to analyze the influence of the ridging process on ridge formation quality. To assess the effects of key parameters on ridge height stability, cross-sectional mesh coordinate points from the simulation output were extracted and fitted. By fixing two factors at their median levels and varying the third, ridge profile curves were generated for different factor levels. This approach provided a basis for optimizing the operating parameters of the ridge–mulching machine. As shown in Figure 17.
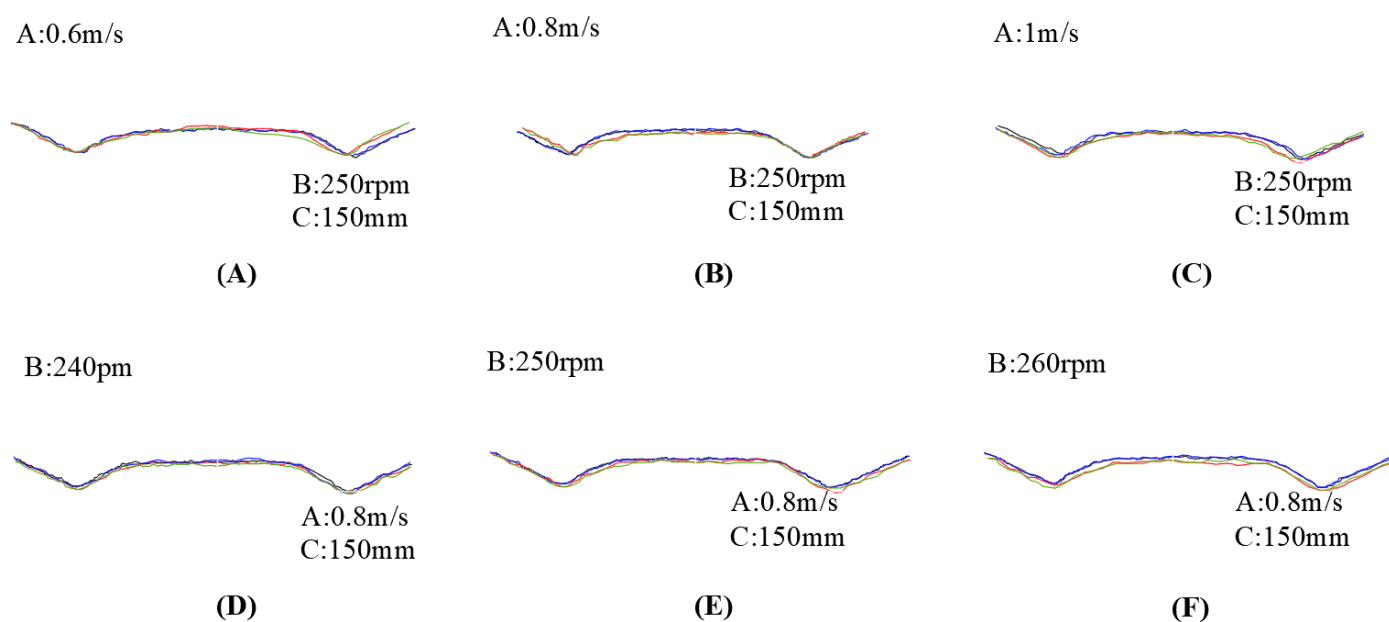

Figure 17. *Cont.*

C:160mm

C:150mm

C:140mm

A:0.8m/s
B:250pm

A:0.8m/s
B:250rpm

A:0.8m/s
B:250rpm
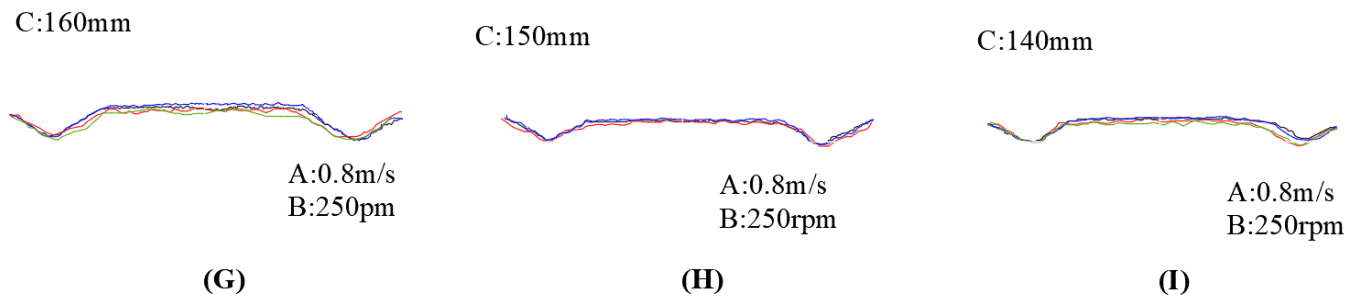
(G)

(H)

(I)

Figure 17. Effects of experimental factors on ridge profile and height. **A**: Effect of forward speed on ridge profile and height; **B:** Effect of blade shaft speed on ridge profile and height; **C:** Effect of ditching depth on ridge height. Black line—ridge profile at the center cross-section for the variable-pitch helical blade shaft; Blue line—ridge profile at 0.5 m from the center cross-section for the variable-pitch helical blade shaft; Red line—ridge profile at the center cross-section for the constant-pitch blade shaft; Green line—ridge profile at 0.5 m from the center cross-section for the constant-pitch blade shaft.

To evaluate the effects of forward speed (A), rotary tiller speed (B), and tillage depth (C) on ridge quality, a response surface methodology (RSM) experimental design was adopted, with ridge height qualification rate and light-receiving surface width qualification rate as evaluation indices. The factor ranges were determined according to the national standard for rotary tillers (GB/T 5668-2017) [40]: forward speed (A), 0.6–1.0 m·s^{-1}; rotary tiller speed (B), 240–260 rpm; and tillage depth (C), 140–160 mm. To ensure the reliability of the simulation results, each test point was subjected to three independent repeated simulations, with the mean value used as the final evaluation indicator. In addition, the dispersion of all output indices was calculated. The results showed that the fluctuations among repeated simulations were minimal; for instance, the standard deviation of ridge height qualification rate was less than ±1%. This indicates that the DEM simulations employed in this study exhibited excellent repeatability and stability. Based on the response surface methodology, the interactive effects of the factors were comprehensively analyzed, and the optimal combination of operating parameters was determined.

Under the yellow-sand substrate condition, a complex coupling relationship was observed among forward speed, rotary tiller speed, and tillage depth. Excessive forward speed tended to destabilize ridge structure; overly high rotary speed exacerbated substrate particle fragmentation, adversely affecting root anchorage; and insufficient tillage depth reduced substrate loosening, restricting root development. The optimized parameter combination identified in this study effectively improved ridge height qualification rates. Compared with conventional moldboard plows or chain-type ridging devices that rely on high-power drive systems, the rotary structure exhibited advantages of mechanical simplicity, high fragmentation efficiency, and stable operation, making it particularly suitable for low-cohesion substrates. To address the tendency of constant-pitch ridging blades to produce loose or collapsed ridges in highly flowable substrates, this study proposed a variable-pitch blade arrangement. By coordinating directional sand-particle stacking paths with controlled dynamic disturbance, the design enhanced ridge density and structural stability, offering both a technical pathway and theoretical foundation for high-quality mechanized ridging under complex substrate conditions.

3.1.2. Ridge Stability and Uniformity Coefficient Analysis

The ridge stability and ridge height uniformity coefficient for each set of simulated experiments were calculated, as shown in Figure 18. The ridge height stability rate was determined using the following equation:

$$F_1 = \frac{Q_0}{Q_1} \times 100\% \tag{32}$$

where F_1 is the ridge height stability rate; Q_0 is the actual ridging height, mm; Q_1 is the theoretical ridging height, mm.
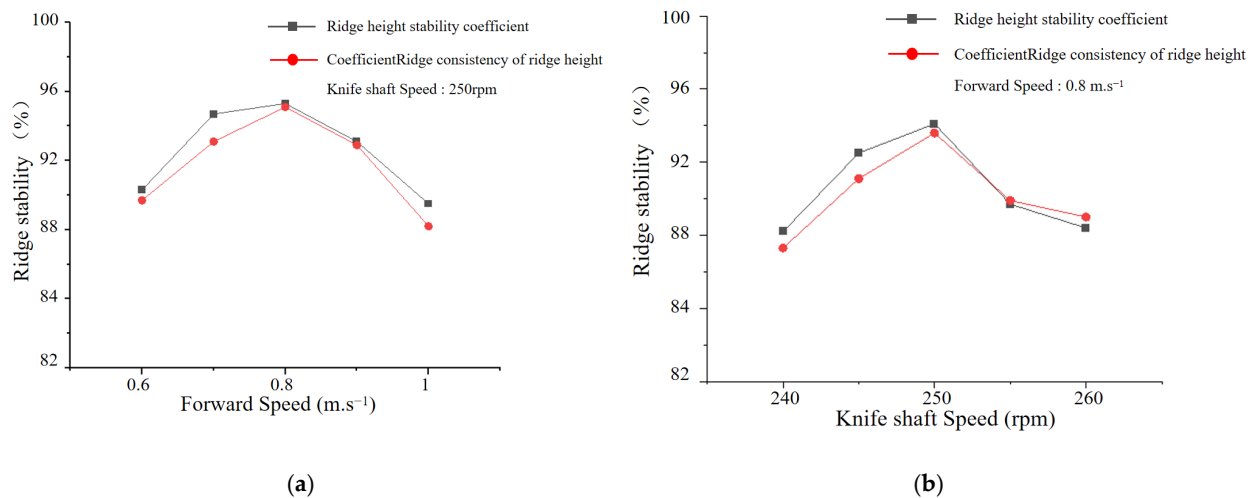

Figure 18. Effect of operating parameters on ridge height stability coefficient and ridge height uniformity coefficient: (**a**) Effect of forward speed; (**b**) Effect of rotary shaft speed.

The crucial threshold for ridge stability in the yellow-sand substrate was determined to be 150 mm of tillage depth. Excessive depth led to a doubling of collapse rate; a rotary shaft speed of 260 rpm achieved a balance between sand-particle migration and centrifugal dispersion; and a forward speed of 0.8 m·s^{-1} ensured adequate working time for the mulching mechanism. Under the synergistic constraints of these three factors, the optimal parameter combination was determined as A = 150 mm, B = 260 rpm, C = 0.82 m·s^{-1}, achieving an average ridge height qualification rate of 95.7%.

From Figure 18a, at a low forward speed of 0.6 m·s^{-1}, the blades maintained sufficient contact with the yellow-sand substrate, achieving effective cutting with minimal disturbance. The substrate was evenly distributed, favoring stable ridge formation. As the forward speed increased from 0.6 to 0.8 m·s^{-1}, the system gradually shifted from a stable to a more disturbed state: the increased kinetic energy enhanced soil particle mobility, leading to stronger turbulence and uneven deposition. This transition marked the beginning of ridge instability, with irregular ridge profiles starting to emerge and stability showing a significant decline. When the speed was further increased to 1.0 m·s^{-1}, the inertial forces applied by the blades intensified, accelerating particle motion, increasing tumbling, and causing irregular deposition. Meanwhile, the reduced contact time between blades and substrate hindered the overcoming of substrate resistance, further lowering stability. Nevertheless, even at this speed, the ridge height uniformity coefficient remained at 88.5%, indicating that substrate flow tended toward stability and the overall structure maintained relative uniformity despite the disturbance.

From Figure 18b, at low rotary shaft speeds, blade cutting energy was insufficient to overcome the cohesive forces of the yellow-sand substrate, causing uneven stress distribution and poor ridge stability. With increasing speed, cutting efficiency improved, allowing the substrate to be rapidly and evenly separated, thus stabilizing ridge structure and improving all stability metrics. In particular, the improvement trend was most evident when the rotary speed was raised from a low level to about 250 rpm, similar to the forward speed case where the range from 0.6 to 0.8 m·s^{-1} represented the critical interval: in both situations, this intermediate stage marked the transition from insufficient cutting to effective separation, resulting in enhanced ridge uniformity and stability before a subsequent decline at higher speeds. At 250 rpm, ridge stability peaked, and ridge height

uniformity showed a marked increase, with both indices exceeding 85%. However, when the speed was further increased to 260 rpm or higher, the intensified impact and friction between blades and substrate caused secondary disturbance and displacement, reducing both stability and uniformity. This observation aligns with previous literature, confirming that excessive rotary speeds can induce secondary particle movement and increase energy consumption. Therefore, the optimal rotary speed should ensure effective cutting while avoiding excessive impact that compromises ridge stability.

Due to its low cohesion and high flowability, the yellow-sand substrate is prone to particle dispersion under rotary tillage disturbance, leading to loose ridges or even collapse. Simulation results revealed that operating parameters significantly influenced ridge stability. The optimal performance was achieved when the forward speed was set at approximately 0.8 m·s^{-1}, the rotary shaft speed at around 250 rpm, and the tillage depth controlled at 150 mm. Under this parameter combination, the substrate underwent orderly deposition with sufficient compaction, resulting in dense, well-shaped, and stable ridges. In contrast, excessively low or high forward speeds, or rotary speeds outside this range, induced uneven particle motion and stacking, leading to edge slippage, deformation, or collapse of the ridge. Furthermore, tillage depths exceeding 150 mm disrupted the integrity of the underlying structure, reducing load-bearing capacity and exacerbating overall instability. These findings demonstrate that a rational matching of forward speed, rotary shaft speed, and tillage depth—particularly the combination of 0.8 m·s^{-1}, 250 rpm, and 150 mm—represents the optimal operating parameters for balancing disturbance intensity and particle deposition, thereby improving ridge uniformity and operational quality.

3.1.3. Traction Force and Energy Efficiency Comparison Between the Designed and Conventional Machines

The traction force and effective field capacity (EFC) of the designed and conventional machines were compared and analyzed. Figures 19 and 20 illustrate the effects of forward speed and tillage depth on traction force and effective field capacity, respectively. Based on the data presented in these figures, the performance differences between the designed machine and the conventional machine under various operational conditions are clearly demonstrated.
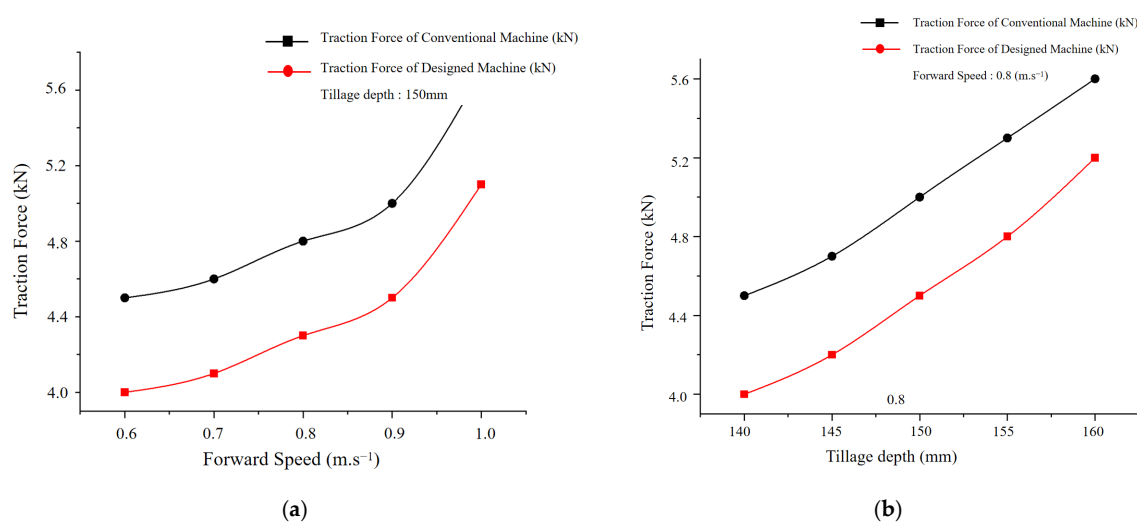

(a)

(b)

Figure 19. Traction Force Comparison Between the Designed and Conventional Machines Under Different Operational Conditions. (**a**) Effect of Forward Speed on Traction Force of Designed and Conventional Machines, with Tillage Depth Fixed at 150 mm. (**b**) Effect of Tillage Depth on Traction Force of Designed and Conventional Machines, with Forward Speed Fixed at 0.8 m/s.
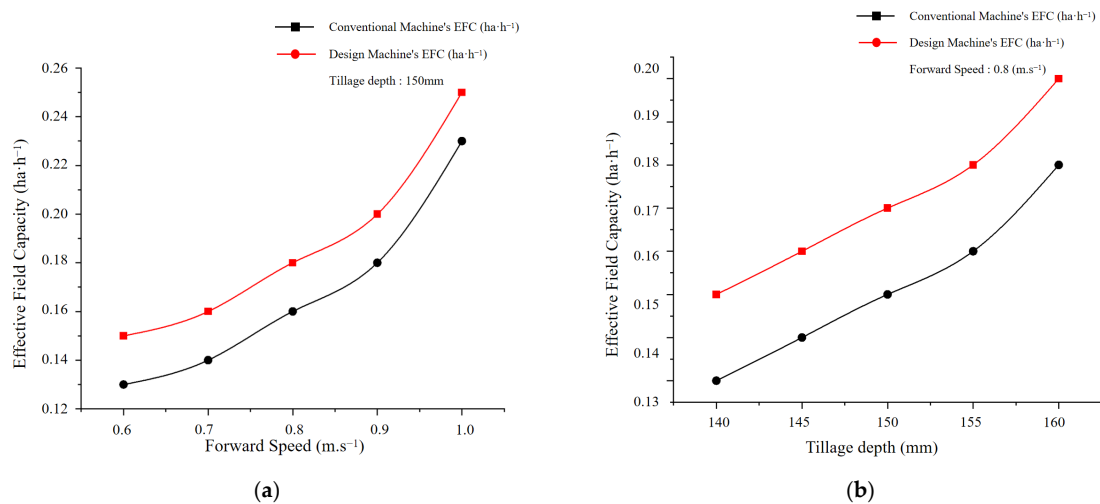
Figure 20. Comparison of Effective Field Capacity (EFC) Between the Designed and Conventional Machines Under Different Operational Conditions. (**a**) Effect of Forward Speed on Effective Field Capacity (EFC) of the Designed and Conventional Machines, with Tillage Depth Fixed at 150 mm. (**b**) Effect of Tillage Depth on Effective Field Capacity (EFC) of the Designed and Conventional Machines, with Forward Speed Fixed at 0.8 m/s.

Traction Force Comparison with Forward Speed.

Figure 19a illustrates the effect of forward speed on traction force, with tillage depth fixed at 150 mm. As the forward speed increases from 0.6 m/s to 1.0 m/s, the traction force of the designed machine increases from 4.0 kN to 5.1 kN, while that of the conventional machine increases from 4.5 kN to 5.7 kN. This change indicates that, as the forward speed increases, the traction force of the designed machine increases at a slower rate than that of the conventional machine. This suggests that the designed machine can more effectively control traction force during operation, reducing energy consumption. The slower increase in traction force of the designed machine shows its lower traction resistance and suggests its potential for improving operational efficiency.

Traction Force Comparison with Tillage Depth.

Figure 19b shows the effect of tillage depth on traction force, with forward speed fixed at 0.8 m/s. As tillage depth increases from 140 mm to 160 mm, the traction force of the designed machine increases from 4.0 kN to 4.8 kN, while that of the conventional machine increases from 4.5 kN to 5.6 kN. Although the traction force of both machines increases as tillage depth increases, the increase in traction force for the designed machine is smaller, indicating that the designed machine can better control traction force during deep tillage, reducing energy consumption and further improving operational efficiency.

Comparison of Effective Field Capacity (EFC) with Forward Speed.

Figure 20a demonstrates the effect of forward speed on effective field capacity (EFC), with tillage depth fixed at 150 mm. As the forward speed increases, the EFC value of the designed machine rises from 0.15 ha/h to 0.25 ha/h, while the EFC value of the conventional machine increases from 0.13 ha/h to 0.23 ha/h. This change indicates that the designed machine is able to significantly improve operational efficiency at higher forward speeds, showing a higher work capacity and energy efficiency. Notably, the operational efficiency of the designed machine increases more significantly as forward speed increases.

Figure 20b shows the effect of tillage depth on effective field capacity (EFC), with forward speed fixed at 0.8 m/s. As tillage depth increases, the EFC value of the designed machine rises from 0.15 ha/h to 0.20 ha/h, while the EFC value of the conventional machine increases from 0.13 ha/h to 0.18 ha/h. This result indicates that the designed machine is able to maintain a higher operational efficiency as tillage depth increases, demonstrating a stronger work capacity.

From the comparative analysis of Figures 19 and 20, it is evident that the designed machine has significant advantages in traction force control and efficiency improvement. The designed machine exhibits a smaller increase in traction force under different operational conditions, particularly when forward speed and tillage depth increase, demonstrating its ability to effectively control traction force and reduce energy consumption. In terms of operational efficiency, the designed machine consistently outperforms the conventional machine, especially at higher forward speeds and greater tillage depths, where it shows higher operational efficiency and energy efficiency.

3.1.4. Response Surface Simulation Results and Analysis

The experimental parameters were set at low, medium, and high levels to design a field experiment and determine the optimal parameter combination. The evaluation indices were ridge height qualification rate (Y_1) and light-receiving surface width qualification rate (Y_2), with a total of 17 simulation trials conducted. The factor coding table and results are presented in Tables 5 and 6.

Table 5. Factor coding table.

Factor	Level	Low Level	High Level	Unit
Forward speed	0.8	0.6	1	$m \cdot s^{-1}$
Rotary shaft speed	250	240	260	rpm
Tillage depth	150	140	160	mm

Table 6. Experimental design and results.

Std	Run	Forward Speed ($m \cdot s^{-1}$)	Rotary Shaft Speed (rpm)	Tillage Depth (mm)	Ridge Height Qualification Rate (%)	Light-Receiving Width Qualification Rate (%)
15	1	1	240	150	86.2 ± 0.6%	83.5 ± 0.8%
8	2	0.8	250	150	95.7 ± 1.0%	92.0 ± 0.6%
13	3	1	250	140	89.1 ± 0.9%	87.6 ± 0.6%
14	4	0.8	250	150	95.6 ± 0.5%	91.3 ± 0.8%
4	5	0.6	250	160	82.4 ± 0.6%	85.1 ± 0.6%
5	6	0.8	260	140	88.3 ± 0.6%	86.9 ± 0.7%
7	7	1	260	150	85.7 ± 0.5%	84.2 ± 0.7%
3	8	0.8	240	160	83.1 ± 0.9%	82.5 ± 0.7%
1	9	0.6	240	150	87.5 ± 0.8%	86.8 ± 0.9%
9	10	0.8	250	150	95.5 ± 0.4%	91.8 ± 0.7%
11	11	1	250	160	78.8 ± 0.5%	80.3 ± 0.8%
6	12	0.8	250	150	95.1 ± 1.0%	91.4 ± 0.8%
16	13	0.8	240	140	90.2 ± 0.5%	88.4 ± 0.6%
12	14	0.8	260	160	81.6 ± 1.0%	81.9 ± 0.7%
2	15	0.6	260	150	86.9 ± 0.6%	85.7 ± 0.6%
10	16	0.8	250	150	94.8 ± 0.6%	91.1 ± 0.5%
17	17	0.6	250	140	91.5 ± 0.7%	89.2 ± 0.8%

Light-receiving width qualification rate.

The theoretical light-receiving width is calculated according to the formula:

$$B_1 = B_s - 240 - n \times 100 \tag{33}$$

where B_1 is the theoretical light-receiving width (mm), B_s is the designed mulch width (mm), and n is the number of sowing rows per mulch strip ($n = 0$ when no holes are punched in the mulch).

The qualification rate of light-receiving width (S_c) was determined as

$$S_c = \frac{N_c}{11 \times m} \times 100\% \tag{34}$$

where S_c is qualification rate of light-receiving width (%), N_c is the total number of measurement points meeting the light-receiving width requirement, and m is the number of mulch strips covered.

The ridge height qualification rate (F_{lg}) was calculated as

$$F_{lg} = \frac{Q_h}{Q_z} \times 100\% \tag{35}$$

where Q_h is the number of ridges meeting the height requirement; Q_z is the total number of ridges measured.

Analysis of variance (ANOVA) results for Y_1 are summarized in Table 7. Factor A (forward speed) and the quadratic term A^2 exhibited highly significant effects on Y_1 ($p < 0.01$), while B^2 and C^2 showed significant effects ($p < 0.05$). The effects of B, C, and the interaction terms (AB, AC, BC) were not statistically significant ($p > 0.05$). The relative importance of the factors and interactions, based on F-values, followed the order: $A > A^2 > C^2 > B^2$. Non-significant terms were excluded from the final regression model by pooling them into the residual error term.

Table 7. Analysis of variance for ridge height qualification rate (Y_1).

Source	Ridge Height Qualification Rate (%)					
	Sum of Squares	df	Mean Square	F-Value	*p*-Value	Significant
Model	464.14	9	51.57	54.01	<0.0001	
A-Forward speed	9.03	1	9.03	9.46	0.0179	*
B-Rotary shaft speed	2.53	1	2.53	2.65	0.1475	
C-Tillage depth	137.78	1	137.78	144.28	<0.0001	**
AB	0.0025	1	0.0025	0.0026	0.9606	
AC	0.3600	1	0.3600	0.3770	0.5586	
BC	0.0400	1	0.0400	0.0419	0.8437	
A^2	87.46	1	87.46	91.58	<0.0001	**
B^2	74.54	1	74.54	78.06	<0.0001	**
C^2	119.73	1	119.73	125.38	<0.0001	**
Residual	6.68	7	0.9549			
Lack of Fit	6.11	3	2.04	14.25	0.0133	
Pure Error	0.5720	4	0.1430			
Cor Total	470.83	16				
R^2			0.9858			
Adjusted R^2			0.9875			

Note: $p < 0.01$ = highly significant (**); $0.01 \leq p < 0.05$ = significant (*).

The ANOVA results for Y_2 are shown in Table 8. Factors A (forward speed), C (tillage depth), and the quadratic terms A^2, B^2, and C^2 had highly significant effects on Y_2 ($p < 0.01$), while the interaction term AC showed a significant effect ($p < 0.05$). In contrast, the effects of B, AB, and BC were not statistically significant ($p > 0.05$). Based on the F-values, the order of factor significance was $A > C > A^2 > B^2 > C^2 > AC$. Non-significant terms were pooled into the residual error term to establish the final regression model describing Y_2.

Table 8. Analysis of variance for light-receiving surface width qualification rate (Y_2).

Source	Light-Receiving Width Qualification Rate (%)					
	Sum of Squares	df	Mean Square	F-Value	*p*-Value	Significant
Model	225.16	9	25.02	138.93	<0.0001	
A-Forward speed	15.68	1	15.68	87.08	<0.0001	**
B-Rotary shaft speed	0.7812	1	0.7812	4.34	0.0758	
C-Tillage depth	62.16	1	62.16	345.20	<0.0001	**
AB	0.8100	1	0.8100	4.50	0.0716	
AC	2.56	1	2.56	14.22	0.0070	*
BC	0.2025	1	0.2025	1.12	0.3242	
A^2	35.96	1	35.96	199.71	<0.0001	**
B^2	52.99	1	52.99	294.26	<0.0001	**
C^2	39.10	1	39.10	217.16	<0.0001	**
Residual	1.26	7	0.1801			
Lack of Fit	0.7125	3	0.2375	1.73	0.2979	
Pure Error	0.5480	4	0.1370			

Source	Light-Receiving Width Qualification Rate (%)					
	Sum of Squares	df	Mean Square	F-Value	*p*-Value	Significant
Cor Total	226.42	16				
R^2				0.9944		
Adjusted R^2				0.9873		

Note: $p < 0.01$ = highly significant (**); $0.01 \leq p < 0.05$ = significant (*).

3.1.5. Response Surface Analysis

The ridge height qualifying rate (F_{lg}) as a function of the three important parameters—forward speed, rotary shaft speed, and tillage depth—was described by a second-order multiple regression equation fitted to the data analysis performed using Design-Expert 13 software. The interactive impacts of these parameters are depicted in the relevant response surface plots. Figures 19 and 20.

$$F_{lg} = 95.34 - 1.06A - 0.5625B - 4.15C + 0.025AB - 0.3AC + 0.1BC - 4.56A^2 - 4.21B^2 - 5.33C^2 \tag{36}$$

Similarly, the second-order regression equation for the light-receiving surface width (S_c) in relation to forward speed, rotary shaft speed, and tillage depth is provided in Equation (31).

$$S_c = 91.52 - 1.40A - 0.3125B - 2.79C + 0.45AB - 0.8AC + 0.225BC - 2.92A^2 - 3.55B^2 - 3.05C^2 \tag{37}$$

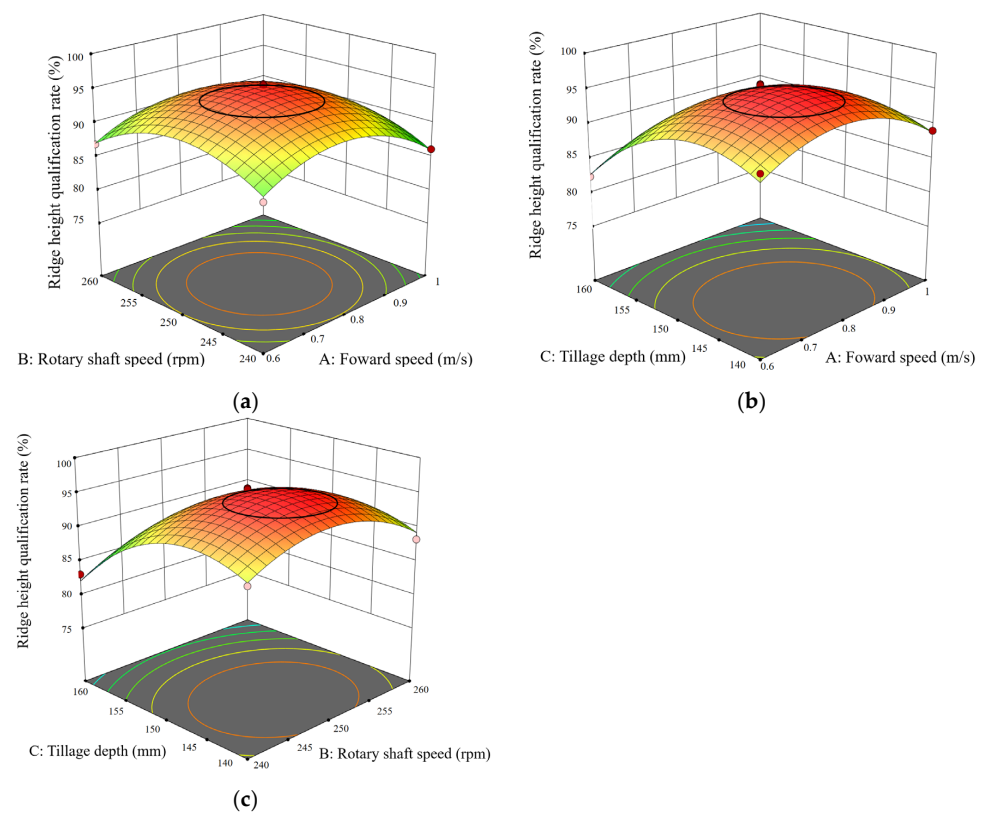The factors' interaction effects on the ridge height qualification rate are depicted in Figure 21.

Figure 21. The contour plots of the response surfaces showing the interactive effects of significant factors on ridge height qualification rate. (**a**) A, B: interactive response surface and contour lines. (**b**) A, C: interactive response surface and contour lines. (**c**) B, C: interactive response surface and contour lines. The colors in the figures represent the ridge height qualification rate: red indicates a higher qualification rate, while green and yellow indicate lower qualification rates.

Figure 21a shows that, when tillage depth and rotary shaft speed are held constant, the ridge height qualification rate initially increases and then decreases with increasing forward speed, with the optimal range being 0.71–0.82 m·s^{-1}. Figure 21b shows that, when tillage depth and forward speed are fixed, ridge height qualification rate first rises and then falls with increasing rotary shaft speed, with the optimal range being 254–260 rpm. Figure 21c shows that, when rotary shaft speed and forward speed are constant, ridge height qualification rate decreases with increasing tillage depth, with the optimal range being 141–150 mm.

The components' combined impacts on the light-receiving surface width qualifying rate are shown in Figure 22.
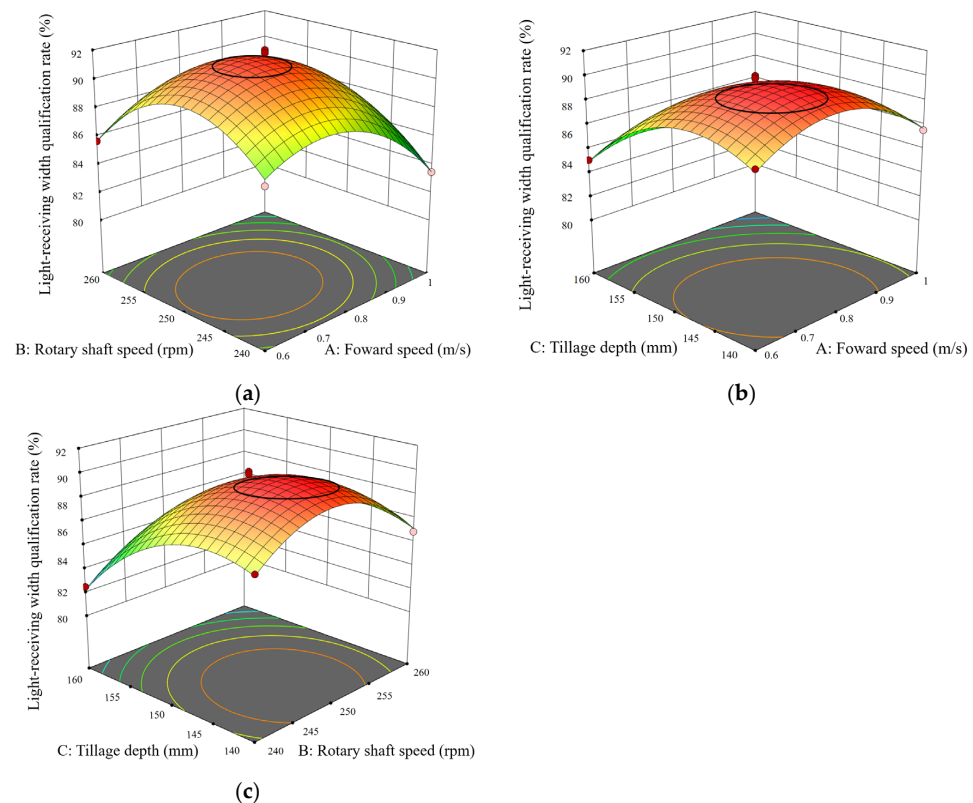

Figure 22. The corresponding plots for the qualification rate of the light-receiving surface width. (**a**) A, B: interactive response surface and contour lines. (**b**) A, C: interactive response surface and contour lines. (**c**) B, C: interactive response surface and contour lines. The colors in the figures represent the ridge height qualification rate: red indicates a higher qualification rate, while green and yellow indicate lower qualification rates.

Figure 22a shows that, when tillage depth and rotary shaft speed are constant, light-receiving surface width qualification rate initially increases and then decreases with increasing forward speed, with the optimal range being 0.648–0.884 m·s^{-1}. Figure 22b shows that, when tillage depth and forward speed are fixed, light-receiving surface width qualification rate first rises and then falls with increasing rotary shaft speed, with the optimal range being 253–265 rpm. Figure 22c shows that, when rotary shaft speed and forward speed are constant, light-receiving surface width qualification rate decreases with increasing tillage depth, with the optimal range being 142–152 mm.

The optimization module of Design-Expert 13 was employed to refine the objective function and constraint conditions based on the regression models, thereby determining the optimal parameter combinations.

$$\begin{cases} minY_1(ABC) \\ maxY_2(ABC) \end{cases} \tag{38}$$

$$\begin{cases} 0.71 \leq A \leq 0.88 \\ 254 \leq B \leq 265 \\ 141 \leq C \leq 152 \end{cases} \tag{39}$$

The final optimization results indicated that the optimal operational stability during rotary tillage and ridge formation was achieved at a tillage depth of 152 mm, a rotary shaft speed of 260 rpm, and a forward speed of 0.82 m·s^{-1}. These values were in close agreement with the optimization analysis and were further validated through field trials, confirming the reliability of the optimization strategy. Field verification also demonstrated that the proposed optimized parameters significantly improved both operational efficiency and the stability of the crop growth environment.

According to experimental and optimization results, ridge profile stability and operating performance were significantly impacted by forward speed, rotary shaft speed, and tillage depth. Forward speed influences the contact duration between the rotary blades and the sandy substrate, thereby affecting the cutting efficiency [41]. Ridge stability is preserved at lower forward speeds because cutting efficiency is increased and substrate disturbance is reduced. On the other hand, ridge stability is compromised by extremely fast forward speeds, which enhance substrate disturbance. Similarly to this, a low rotary shaft speed causes an uneven force distribution because there is not enough cutting energy to overcome the cohesive forces of the sandy substrate; on the other hand, an excessively high rotary shaft speed causes secondary disturbance and substrate displacement, which lowers operational effectiveness. Therefore, the optimal speed range should be determined by comprehensively considering substrate conditions and operational efficiency.

Analysis of tillage depth showed that a moderate depth is favorable for maintaining ridge stability [42]. A shallow depth may result in insufficient loosening of the substrate, leading to poor ridge quality; whereas an excessively deep depth increases disturbance and draft resistance, reducing ridge stability. Previous studies have indicated that the synergistic interaction between tillage depth and rotary shaft speed is critical for operational performance, as an appropriate combination can effectively balance substrate disturbance and ridge stability [43].

Compared with existing literature, the optimized results of this study further confirm the importance of appropriate forward speed and rotary shaft speed in improving operational outcomes. Moreover, the optimized tillage depth helps avoid excessive substrate disruption, enhances substrate stability, and ultimately improves operational efficiency and the quality of the crop growth environment.

3.2. Field Test Results Analysis

The experimental procedure in this study strictly followed the Technical Specification for Mechanized Ridge Formation with Full-Film Mulching (NY/T 2704-2015). Field trials were conducted to verify the structural rationality of each component of the self-propelled ridge-forming and film-mulching machine.

During operation, the tractor advanced at a forward speed of 0.82 m·s^{-1} with a rotary tillage depth of 150 mm. To evaluate the performance of the rotary tillage ridge-forming machine in producing qualified ridges and furrows, several key parameters were measured and statistically analyzed, including the actual ridge height, actual ridge top width, and the damaged area of the light-receiving surface.

The measurement procedure was as follows: a standard 30 m test strip was selected, and the machine parameters were set according to the designed ridge height of 20 cm. Following the operation, three measurement points were established at each distance position (0 m, 10 m, 20 m, and 30 m) to enhance measurement reliability, and the mean value was obtained from repeated measurements.

The average ploughing depth *a* within the operating row is calculated as

$$a = \frac{\sum_{i=1}^{n} a_i}{n} \tag{40}$$

where *a* is the average ploughing depth within the operating row, cm; a_i is the ploughing depth at the i-th measurement point within the row, cm; *n* is the total number of measurement points in the row.

The standard deviation *S* of the ploughing depth is calculated as

$$S = \frac{\sum_{i=1}^{n} (a_i - a)^2}{\sqrt{n-1}} \tag{41}$$

$$V = \frac{S}{a} \times 100\% \tag{42}$$

$$U = 1 - V \tag{43}$$

where *S* is the standard deviation of ploughing depth, cm; *V* is the coefficient of variation of ploughing depth, %; *U* is the stability coefficient of ploughing depth, dimensionless.

The damage rate S_p of the light-receiving surface is calculated as

$$S_p = \frac{\sum S_a}{S_y} \times 100\% \tag{44}$$

where S_p is the damage rate of the light-receiving surface, %; S_a is the damaged area of the light-receiving surface at the measurement point, cm^2; S_y is the effective light-receiving surface area, cm^2.

During the ridge-forming process, maintaining stability coefficients for ridge height, ridge spacing, and ridge surface flatness within the range of 90–95% is essential to ensure both the stability of the crop growth environment and improved production efficiency (See Table 9). Field experiments revealed slight undulations in the working plots. To accommodate such topographical variations, minor manual steering adjustments of the tractor were implemented, effectively reducing the impact of terrain irregularities on ridge stability. These results suggest that the integrated machine improves operational efficiency and reduces the number of traversals. While the tool-level energy may not decrease, the system-level energy consumption is reduced by consolidating operations. As discussed in Section 2.5, energy estimates have been provided based on power usage and effective field capacity (EFC). Further testing is needed to validate these estimations against conventional equipment. The variable pitch roller design demonstrates significant advantages for loose soils such as sandy soils with high flowability, effectively avoiding the instability and looseness of ridges caused by traditional fixed-pitch rollers. However, the advantages of the variable pitch roller are less pronounced in moist or clayey soils, requiring adjustments to operating parameters based on specific soil types. For a ridge length of 100 m, traditional methods require multiple passes to complete all operations, whereas this machine completes the task in a single pass, with an estimated savings of more than 30% in time and fuel consumption. Due to the lack of a comparison with traditional machinery, this study can only evaluate the machine's performance in absolute terms, without quantifying the improvement over conventional equipment, which is a limitation of the experimental design.

During the field experiments, the drip tape was laid simultaneously with the mulching operation, and the overall placement performance was satisfactory. The results showed that the drip tape was uniformly positioned along the ridge centerline, maintaining a straight alignment in the longitudinal direction without noticeable lateral deviation or irregular

burial depth. This indicates that the machine was able to stably guide the drip tape to the ridge top and fix it under the mulch, effectively preventing common problems such as displacement or twisting. These findings further confirm the operational reliability of the machine under multi-process integration and provide a uniform irrigation pathway for subsequent crop cultivation.

Table 9. Field Test Results.

Parameter	Unit	Standard	Data
Tillage depth	m	≥0.08	0.15
Tillage depth stability	%	≥85	93.7
Ridge height stability	%	≥85	94.3
Ridge top width qualification rate	%	≥70	88.9
Ridge spacing qualification rate	%	≥75	100
Yellow-sand substrate firmness	kPa		152.1
Film edge width	mm	≥70	75.2
Light-receiving surface width	mm	≥75	598.6
Light-receiving surface damage rate	%	≥75	2.1%

Furthermore, factors such as yellow-sand substrate moisture content, substrate type, and tillage depth also influence ridge quality. These variables can cause subtle fluctuations in ridge morphology. Therefore, operational parameters must be periodically adjusted during field trials to maintain consistent ridge quality under varying conditions (see Figure 23).

Figure 23. Field experiment of ridge forming and mulching in a solar greenhouse.

Analysis of the field trial data further confirmed the relationship between parameter adjustment and ridge stability. When the stability coefficients for ridge height, ridge spacing, and ridge surface flatness exceeded 90%, both ridge stability and the substrate's water-retention capacity improved significantly. Additionally, fine-tuning tractor operation enhanced adaptability to irregular plot conditions, thereby enabling standardized ridge formation. This process plays a critical role in improving mechanized operation efficiency and optimizing the utilization of the yellow-sand substrate, providing a robust foundation for future equipment standardization and optimization.

4. Conclusions

1. This study focused on the yellow-sand substrate environment in the Northwest region of China and designed and optimized a ridge-forming and mulching machine specifically adapted for solar greenhouse cultivation systems. The machine integrates rotary tillage, ridge formation, and plastic film mulching functions, aiming to enhance

mechanized crop production efficiency. Through theoretical analysis and EDEM simulations, a variable-pitch helical ridge-forming cutter roller was developed, and the lateral throwing trajectory of the yellow-sand substrate was optimized. Simulation results identified the effects of forward speed, rotary shaft speed, and tillage depth on ridge stability, providing a theoretical basis for operational parameter optimization. In addition, the mulching mechanism adopted a rotatable slider design, and by analyzing the mulching position and pressure roller force distribution, the mulching performance was improved. Experimental results demonstrated that the optimized machine enhanced operational efficiency and ridge stability in the yellow-sand substrate environment, providing a favorable growth environment for crops.

2. Based on EDEM simulation analysis, a central composite design (CCD) experiment was conducted using forward speed, rotary shaft speed, and tillage depth as experimental factors, with ridge height qualification rate and light-receiving surface width qualification rate as evaluation indices. Regression equations were established to determine the optimal operational parameters: forward speed of 0.82 m s^{-1}, rotary shaft speed of 260 rpm, and rotary tillage depth of 150 mm. Results indicated that, under identical conditions, the variable-pitch helical arrangement transported a greater amount of yellow-sand substrate compared to the constant-pitch arrangement, thereby achieving superior ridge formation performance.

3. Field trials confirmed the outstanding performance of the ridge-forming and mulching machine. The measured ridge top width, ridge base width, ridge height, ridge spacing, and plastic film edge width were 598.6 mm, 802.3 mm, 202.4 mm, 1002.8 mm, and 75.2 mm, respectively, with ridge dimension stability coefficients all exceeding 93.7%. This study estimates the traction energy using power consumption and effective field capacity (EFC), and provides an initial estimation of the traction force and operational efficiency for both the designed and conventional machines. Through comparative analysis, the advantages of the designed machine in reducing traction force and improving operational efficiency have been demonstrated. Future experiments will further validate the accuracy of these estimations through traction sensors and energy efficiency measurements under real-world operating conditions, providing additional data support for the practical application of the designed machine. The substrate firmness reached 152.1 kPa. All parameters met the agronomic requirements for tomato ridge formation. The proposed design effectively improved operational efficiency, enhanced tomato yield and quality, ensured efficient resource utilization, and contributed to environmental protection and sustainable agricultural development.

Author Contributions: Y.Z.: Writing—original draft, Writing—review & editing, Methodology, Software, Validation, Data curation, Formal analysis, Visualization. J.B.: Writing—review & editing, Validation, Data curation. W.L.: Conceptualization, Supervision, Project administration, Funding acquisition, Writing—review & editing. J.X.: Methodology, Formal analysis, Writing—review & editing, Project administration. L.W.: Resources, Validation, Writing—review & editing, Project administration, Funding acquisition. X.W.: Conceptualization, Methodology, Supervision, Project administration, Funding acquisition, Writing—review & editing. C.H.: Resources, Validation, Investigation, Project administration. All authors have read and agreed to the published version of the manuscript.

Data Availability Statement: The original contributions presented in this study are included in the article. Further inquiries can be directed to the corresponding author.

Conflicts of Interest: The authors declare that they have no known competing financial interests or personal relationships that could have appeared to influence the work reported in this paper.

References

1. Xie, Y.; Dang, X.; Meng, Z.; Jiang, H.; Li, X.; Zhou, R.; Zhou, D.; Liu, X.; Ding, J.; Wu, X.; et al. Wind and sand control by an oasis protective system: A case from the southeastern edge of the Tengger Desert, China. *J. Mt. Sci.* **2019**, *16*, 2548–2561. [CrossRef]
2. Zhang, G.L. Mulching cultivation technique for small ridge–furrow planting of tomatoes in yellow sand substrate in Gobi solar greenhouses. *Agric. Eng. Technol.* **2022**, *42*, 55–57. [CrossRef]
3. Song, Y.; Xu, J.; Zhang, S.; Xing, J.; Wang, L.; Wang, X.; Hu, C.; Li, W.; Tan, Z.; Cheng, Y. Optimizing water–fertilizer coupling across different growth stages of tomato in yellow sand substrate: Toward enhanced yield, quality, and resource use efficiency. *Plants* **2025**, *14*, 936. [CrossRef] [PubMed]
4. Ma, X.C.; Zhou, Y.; Liu, Q.; Xuan, Z.; Chen, M.; Zhang, K.; Wang, X.; Tan, Z. Effects of water–fertilizer coupling on photosynthetic fluorescence characteristics, yield, and quality of cucumber cultivated in a composite substrate of yellow sand and furnace slag. *Xinjiang Agric. Sci.* **2022**, *59*, 597–608. [CrossRef]
5. Liu, C.C.; Huang, C.Y.; Wang, D.W. Effects of integrated water and fertilizer management in yellow sand substrate on yield and quality of tomato. *Xinjiang Agric. Sci.* **2020**, *57*, 2250–2259. [CrossRef]
6. Zhou, Y.; Chen, M.M.; Liu, Q.; Ma, X.; Geng, Y.; Yang, P.; Ma, G.; Xuan, Z. Effects of different ratios of yellow sand and furnace slag substrates on growth and physiological characteristics of greenhouse cucumber plants. *J. Agric. Sci. Technol. China J.* **2019**, *21*, 117–124. [CrossRef]
7. Gao, Q.; Hu, H.; Chen, Q.; Chen, Y.; Guan, C.; Yang, Y. Current status and development trend of mechanized ridging technology for facility vegetable production in China. *China Veg.* **2016**, *5*, 4–7.
8. Wang, J. Development of a Ridging, Mulching, and Pipe-Laying Integrated Machine for Greenhouse Cultivation. Master's Thesis, Shenyang Agricultural University, Shenyang, China, 2024. [CrossRef]
9. Qiu, W.; Liu, Y.; Liu, Q.; Hao, Y.; Chen, J.; Lei, R.; Wang, X. Design and test of greenhouse fine spiral flame soil disinfection and ridge forming machine. *Trans. Chin. Soc. Agric. Eng.* **2025**, *41*, 1–10. [CrossRef]
10. Chen, X.; Chen, M.; Liu, M.; Li, Y.; Yang, D.; Wu, H. Design and experiment of sweet potato ridging and forming machine. *Agriculture* **2023**, *13*, 1641. [CrossRef]
11. Zeng, Z.W.; Ma, X.; Cao, X.L.; Li, Z.; Wang, X. Application status and prospects of the application of the discrete element method in agricultural engineering research. *Trans. Chin. Soc. Agric. Mach.* **2021**, *52*, 1–20. [CrossRef]
12. Zheng, J.; Wang, L.; Wang, X.; Shi, Y.; Yang, Z. Parameter calibration of cabbages (Brassica oleracea L.) based on the discrete element method. *Agriculture* **2023**, *13*, 555. [CrossRef]
13. Bembenek, M.; Buczak, M.; Baiul, K. Modelling of the fine-grained materials briquetting process in a roller press with the discrete element method. *Materials* **2022**, *15*, 4901. [CrossRef] [PubMed]
14. Aikins, K.A.; Ucgul, M.; Barr, J.B.; Awuah, E.; Antille, D.L.; Jensen, T.A.; Desbiolles, J.M.A. Review of Discrete Element Method Simulations of Soil Tillage and Furrow Opening. *Agriculture* **2023**, *13*, 541. [CrossRef]
15. Zhao, Z.; Wu, M.; Jiang, X. A Review of Contact Models' Properties for Discrete Element Simulation in Agricultural Engineering. *Agriculture* **2024**, *14*, 238. [CrossRef]
16. Zeng, Y.; Chen, C.; Quan, W.; Xie, S.; Shi, F.; Ma, Z.; Wu, M. Calibration Parameter of Soil Discrete Element Based on Area Difference Method. *Agriculture* **2023**, *13*, 648. [CrossRef]
17. Li, G.; Aili Hasimu; Kang, X.S.; Yu, G.; Zhang, G. Parameter optimization of the spiral soil-covering drum for a plastic-film seeder. *Trans. Chin. Soc. Agric. Eng.* **2003**, *6*, 135–138.
18. Han, D.L.; Hu, J.R.; Liu, H.R.; Ren, L.; Zhou, M.; Yang, Q.; Li, B.; Chen, X. Calibration and testing of discrete element contact model parameters for wet sandy soil particles. *Trans. Chin. Soc. Agric. Eng.* **2025**, *41*, 70–78.
19. Song, Y.; Xu, J.; Zhang, S.; Xing, J.; Wang, L.; Wang, X.; Hu, C.; Li, W. Modeling of sand-cultivated substrate for Gobi facility agriculture and validation of trenching test. *Sci. Rep.* **2025**, *15*, 9536. [CrossRef]
20. Du, X.; Liu, J.; Zhao, Y.; Zhang, C.; Zhang, X.; Wang, Y. Design and Test of Discrete Element-Based Separation Roller Potato–Soil Separation Device. *Agriculture* **2024**, *14*, 1053. [CrossRef]
21. Dai, F.; Pan, H.; Zhou, W.; Tang, H.; Wang, Q.; Li, W.; Wang, J. Analysis of Maize Planting Mode and Simulation and Optimization of Ridging and Fertilization Components in Arid Area of Northwest China. *Agriculture* **2024**, *14*, 1360. [CrossRef]
22. Li, J.; Sun, W.; Wang, H.; Wang, J.; Simionescu, P.A. An Integrated Potato-Planting Machine with Full-Film Mulching and Ridged Row Soil Covering. *Agriculture* **2024**, *14*, 860. [CrossRef]

23. Lu, N.; Kim, T.-H.; Sture, S.; Likos, W.J. Tensile strength of unsaturated sand. Tensile strength of unsaturated sand. *J. Eng. Mech.* **2009**, *135*, 1410–1419. [CrossRef]

24. Yang, Z.; Zhang, K.; Zhang, Y.; An, J. Discrete element method–multibody dynamics coupling simulation and experiment of rotary tillage and ridging process for chili pepper cultivation. *Agronomy* **2024**, *14*, 446. [CrossRef]

25. Zhang, R.; Han, D.; Ji, Q.; He, Y.; Li, J. Study on sandy soil parameter calibration method in DEM simulation. *Trans. Chin. Soc. Agric. Mach.* **2017**, *48*, 49–56. [CrossRef]

26. Zhang, B.; Chen, J.; Zhu, Y. Improved Design and Simulation of an Integrated Ridge-Breaking Earth Cultivator for Ratoon Sugarcane Fields. *Agriculture* **2024**, *14*, 1013. [CrossRef]

27. Zhu, Z.; Li, B.; Xu, Z.; Xie, Y.; Zhu, X. An innovative approach to plastic mulch film modeling based on the discrete element method. *Sci. Rep.* **2025**, *15*, 23967. [CrossRef]

28. Liu, Q.; Sun, W.; Wang, H.; Meng, Y. Design and field test of a leaping-type soil-covering device on plastic film. *Agriculture* **2023**, *13*, 1680. [CrossRef]

29. Wei, Q.; Zhang, Z.Y.; Wang, C.; Chen, Y.; Zhang, Z.M. Crack closure and flow regimes in cracked clay loam subjected to different irrigation methods. *Geoderma* **2020**, *358*, 113978. [CrossRef]

30. Song, X.; Dai, F.; Zhang, X.; Chen, H.; Zhang, F.; Zhao, W. Numerical analyses ridge-forming for whole film-mulching and double ridge–furrow, a discrete element method. *Comput. Electron. Agric.* **2023**, *215*, 108364. [CrossRef]

31. Yang, S.; Sultan, C. Deployment of foldable tensegrity–membrane systems via transition between tensegrity configurations and tensegrity–membrane configurations. *Int. J. Solids Struct.* **2019**, *160*, 103–119. [CrossRef]

32. Wright, A. Tyrel Soil Interaction Modelling Within a Virtual Proving Ground Environment. Ph.D. Thesis, Cranfield University, Shrivenham, UK, 2012.

33. Jiang, D.; Chen, X.; Yan, L.; Yang, J.; Li, Y. Mechanical and friction properties of agricultural plastic film during autumn harvest of cotton in Xinjiang, China. *Environ. Sci. Pollut. Res.* **2023**, *30*, 89238–89252. [CrossRef]

34. Zhao, Q.; Dai, F.; Shi, R.; Zhao, W.; Xu, P.; Deng, H.; Pan, H. Effect of operating parameters on the mulching device wear behavior of a ridging and mulching machine. *Lubricants* **2024**, *12*, 19. [CrossRef]

35. Wang, X.L.; Zhong, X.K.; Geng, Y.L.; Wei, Z.; Hu, H.; Geng, D.; Zhang, X. Parameter Calibration of no-tillage soil parameters based on a discrete element nonlinear elastoplastic contact model. *Trans. Chin. Soc. Agric. Eng.* **2021**, *37*, 100–107. [CrossRef]

36. Yan, D.; Yu, J.; Wang, Y.; Zhou, L.; Tian, Y.; Zhang, N. Soil particle modeling and parameter calibration based on discrete element method. *Agriculture* **2022**, *12*, 1421. [CrossRef]

37. Tan, Z.; Zheng, Y.; Shu, S.; Xiong, R.; Du, J.; Li, C. Protected tomato cultivation model using yellow-sand substrate in southern Xinjiang. *North. Hortic.* **2020**, *22*, 166–169.

38. Shi, L.R.; Wu, J.M.; Zhao, W.Y.; Sun, W.; Zhang, F.; Sun, B. Establishment and parameter verification of a uniaxial compression model for farmland soil based on the discrete element method. *J. China Agric. Univ.* **2015**, *20*, 174–182. [CrossRef]

39. Turek, M.E.; Armindo, R.A.; Wendroth, O.; Dos Santos, I. Criteria for the estimation of field capacity and their implications for the bucket type model. *Eur. J. Soil Sci.* **2018**, *70*, 278–290. [CrossRef]

40. *GB/T 5668-2017*; Rotary Tiller. China National Machinery Industry Corporation: Beijing, China, 2017.

41. Sahu, R.K.; Raheman, H. An approach for draft prediction of combination tillage implements in sandy clay loam soil. *Soil Tillage Res.* **2006**, *90*, 145–155. [CrossRef]

42. Gao, J.; Zhang, X.S.; Chen, X.Y. Design and experimental study of the pressing and shaping device for a sweet potato ridging and shaping machine based on EDEM. *Agric. Eng.* **2024**, *14*, 95–99. [CrossRef]

43. Liu, C.A.; Zhou, L.M.; Jia, J.J.; Wang, L.J.; Si, J.T.; Li, X.; Pan, C.C.; Siddique, K.H.M.; Li, F.M. Maize yield and water balance is affected by nitrogen application in a film–mulching ridge–furrow system in a semiarid region of China. *Eur. J. Agron.* **2014**, *52*, 103–111. [CrossRef]